



TECHNICAL ARTICLE

Defect-Correlated Vickers Microhardness of Al-Si-Mg Alloy Manufactured by Laser Powder Bed Fusion with Post-process Heat Treatments

Emanuela Cerri, Emanuele Ghio , and Giovanni Bolelli

Submitted: 1 December 2021 / Accepted: 25 March 2022

Laser powder bed fusion is an additive manufacturing process characterized by different advantages like the manufacture of samples with complex geometry without the use of tools and/or molds. Generally, the manufactured samples are characterized by high tensile strengths which, however, can be affected by the presence of defects due to the unoptimized process parameters. In a large applications field, a low density of the as-built AlSi10Mg samples is a very important parameter to be considered, e.g., due to both the loss of the tensile strengths correlated with a premature failure of the samples and the increase in time and costs associated with the manufacturing process. In addition, different post-process heat treatments can increase these effects leading to an ineffective manufacturing process. In this scenario, the present work shows the analysis of spherical and lack-of-fusion pores induced by the laser powder bed fusion process on the AlSi10Mg samples and their variations after different heat treatments (direct aging and T6). At the same time, the influence of pores on the Vickers microhardness and the tensile properties has been studied in the same AlSi10Mg samples (bars and billets) that were printed with single- and double-laser machine setup. Different process parameters were also analyzed and compared. The study was supported by the microstructural and pore analysis performed by optical microscopy along the XZ plane (build direction) and the XY plane. Finally, the greatest effects of pores were observed on the Vickers microhardness values; in fact, two different relationships between microhardness and density variation are discussed. The T6 heat treatment leads to a rounding of the pores already formed in the as-built samples and to a formation of new small pores.

Keywords AlSi10Mg laser powder bed fusion, gas pores, heat treatments, mechanical properties, process parameters, Vickers microhardness

1. Introduction

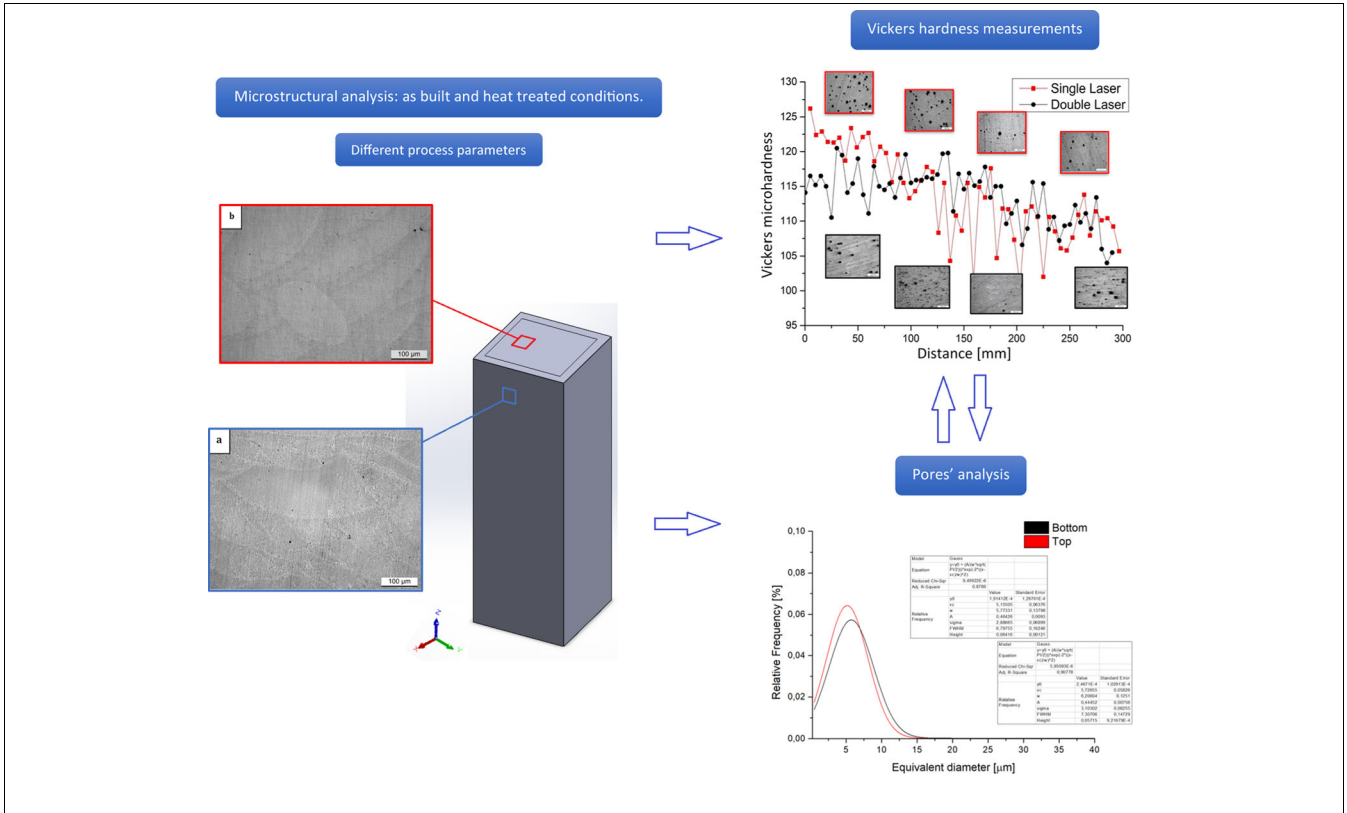
AlSi10Mg alloy is a hypoeutectic aluminum alloy based on Al-Si-Mg ternary system, characterized by low density, low thermal expansion and excellent mechanical properties, which make it optimal for aerospace and automotive fields. The production of high-quality metallic powders allows the use of the AlSi10Mg alloy in additive manufacturing (AM) processes obtaining good-quality samples. The as-built samples show a

very fine microstructure where the α -Al matrix is surrounded by the network of eutectic silicon that makes the AlSi10Mg much resistant, but less ductile (Ref 1, 2). Cabrini et al. (Ref 3), who analyzed the selective laser-melted AlSi10Mg alloy, highlighted the presence of brittle and acicular β -Al₃FeSi phases in the as-built samples, and ϵ -Mg₂Si precipitates after heat treatments at temperatures between 200 and 500 °C. Cao et al. (Ref 4) showed that the brittle and acicular β phases are responsible for the decrease in mechanical properties in Al-Si alloy. On the other hand, Cerri et al. (Ref 5) emphasized the effects of the Mg₂Si phases in increasing the UTS and the yield strength. In that study, the precipitation hardening phenomena were induced in as-built samples by the pre-heated build platform. Despite the metallurgical aspect, the mechanical behavior can be conditioned by the process parameters optimization for the AM technology due to the defects generated within the manufactured parts.

In selective laser melting (SLM), also known as a L-PBF (laser powder bed fusion) process, samples are manufactured by scanning metallic powder layers with a laser beam, which is characterized by a specific laser power (P , [W]), depending on the type of machine. During the printing process, the physical object is built layer by layer on the build platform to its maximum height following a CAD (Computer-Aided Design) project (Ref 6). L-PBF is characterized by four main process parameters: laser power, scan speed (\vec{v}_s , [$\frac{\text{mm}}{\text{s}}$]), layer thickness (t , [mm]), and hatch spacing (h , [mm]) that define the energy density function ($\psi = \frac{P}{v_s h t}$, [$\frac{\text{J}}{\text{mm}^3}$]). As widely discussed in the literature, process parameters may explain variations in

Emanuela Cerri and **Emanuele Ghio**, Department of Engineering and Architecture, University of Parma, Via G. Usberti 181/A, Parma, Italy; and **Giovanni Bolelli**, Department of Engineering “Enzo Ferrari”, University of Modena e Reggio Emilia, Via Pietro Vivarelli 10/1, 41125 Modena, Italy; InterMech MO.RE. Centro Interdipartimentale per la Ricerca Applicata e i Servizi nel Settore della Meccanica Avanzata e della Motoristica, Università di Modena e Reggio Emilia, Via Pietro Vivarelli 2, 41125 Modena, Italy; and Local Unit, Consorzio Interuniversitario Nazionale per la Scienza e Tecnologia dei Materiali (INSTM), Local Unit, Università di Modena e Reggio Emilia, Via Pietro Vivarelli 10/1, 41125 Modena, Italy. Contact e-mails: emanuela.cerri@unipr.it emanuele.ghio@unipr.it.

Graphic Abstract



UTS (ultimate tensile strength), σ_y (yield strength) and ductility through their influence on both the microstructure and the presence of pores. As reported in the study of Wang et al. (Ref 7), with the increase in energy density from 25 to 60 $\frac{\text{J}}{\text{mm}^3}$, the relative sample density tends to increase from 92.0 to 93.0%, while at $\psi = 10 \frac{\text{J}}{\text{mm}^3}$ it settles around 97.5%. Consequent to these variations, UTS and σ_y increase. Similar results were obtained by Hyer et al. Ref 8: relative material density increased when energy density was in the range between 25 and 60 $\frac{\text{J}}{\text{mm}^3}$, while it decreased from 99.5 to 93% for energy density up to 100 $\frac{\text{J}}{\text{mm}^3}$.

In this scenario, Aboulkhair et al. Ref 9 showed how the process parameters' variation can affect the pores' formation in SLMed AlSi10Mg. They affirmed that one of the most effective parameters is the hatch spacing h because a lack of overlap between two adjacent laser tracks is generated on the XY plane if h increases. Moreover, another problem is related to the layer thickness t that must be reduced (if the hatch spacing is increased) to satisfy the intra-layer cohesion. Tang et al. (Ref 10) proposed Eq 1 to verify whether the overlap between adjacent molten pools is sufficient:

$$\left(\frac{h}{W}\right)^2 + \left(\frac{t}{D}\right)^2 \leq 1 \quad (\text{Eq 1})$$

where h and t are hatch spacing and layer thickness [mm], as defined above, while W is the melt pool width [mm] and the D the melt pool depth [mm]. In the same context, different combination of the scan speed and the laser power can decrease

the density due to the lack of a perfect fusion and the consequent non-adherence between the new layer and the previously scanned layer. Bai et al. (Ref 11) show the decrease in density using a combination of high scan speed and low laser power due to the inability of the laser beam to provide adequate melting energy.

Other authors focused their attention on the defects generated in as-built samples manufactured by L-PBF process. Anderson et al. (Ref 12) showed how the presence of different amounts of trapped gas within the gas atomized powder and the satellites on the particles' surface is related to the density. In the latter case, the presence of satellites can induce flowability problems during powder deposition causing a density decrease in the manufactured sample. Instead, Shi et al. (Ref 13) highlighted the effects induced by the pre-heated build platform on the density of AlSi10Mg samples manufactured with different energy density values. The results show a slight increase in density with increasing the build platform temperature from 35 to 200 °C and using an energy density of 77 $\frac{\text{J}}{\text{mm}^3}$. On the other hand, the same authors concluded that the variation in the energy density function induces a greater effect on pores' formation than the pre-heating temperature of the build platform. Focusing on the mechanical properties, an interesting study about pores and their effects was conducted by Tiwari et al. (Ref 14). The authors showed a decrease in UTS and yield strength of about 46 and 17%, respectively, due to the relative density decrease from 99.2 to 95.5%. The maximum effect was shown on elongation, which decreased by 80%. On

the other hand, pores are critical defects that dominate the fracture mechanism and, consequently, the fatigue life, during a fatigue test (Ref 15). Xu et al. (Ref 16) highlighted that pores generate a stress/strain concentration in the material around their surface; this effect increases with pore size. In addition, the stress/strain concentrations increase if the distance between two pores is lower than their radius by considering the perpendicular direction to the load axis. Furthermore, pores with an irregular shape are characterized by higher stress concentration than spherical ones as analyzed by (Ref 17).

In this scenario, the aim of the present manuscript is to study the 2D statistical distribution of pores within different 300 mm-high AlSi10Mg bars and billets manufactured via L-PBF, before and after different post-process heat treatments. In addition, the effects induced by pores and heat treatments on Vickers microhardness were studied. Finally, the results were also compared to those by Cerri et al. (Ref 5), who analyzed AlSi10Mg SLMed bars characterized by a lower layer thickness than was used in the present work and a hatch spacing of 170 μm .

2. Material and Methods

Pre-alloyed gas-atomized AlSi10Mg powder, with a size distribution between 20 and 60 μm , was used for the L-PBF process. The chemical composition of the powder is reported in Table 1.

Six bars and three billets, from which the tensile samples were obtained, were manufactured using an SLM280TM (SLM Solutions Group AG, Lübeck, Germany) machine equipped with 2 \times 400 W IPG fiber lasers and a build platform of 280 \times 280 mm². This machine setup allows to obtain two different zones as shown in Fig. 1(a) where a schematic representation of the manufactured samples was illustrated. The red zones are characterized by a single-laser (SL) process, while the yellow zones by two lasers (DL) that work in parallel. During the printing process, argon was used to reduce the oxygen content below 0.2%.

The bars (10 \times 10 \times 300 mm³) and billets (10 \times 100 \times 300 mm³) were printed according to the scan strategy shown in Fig. 1(b) where the layer “ $n + 1$ ” was rotated by 67° compared to the previous layer “ n ”.

The L-PBF process used the skin-core strategy for printing where each layer was formed by the external frame (EF), which is scanned first, and the area inside the frame or center zone (CM) is represented by the dotted arrows in Fig. 1(b) and scanned then to the EF. Each arrow that schematically represents a laser scan track is inclined by 56.5° (α angle), and all are arranged parallel to each other. For better characterization, all bars were divided along the height into two parts, namely the top (heights from 150 to 300 mm) and the bottom (from 0 to 150 mm). In addition, the EF and the CM zones were analyzed along the XZ plane (EF_{XZ}, CM_{XZ}) and the XY plane (EF_{XY}, CM_{XY}) as highlighted through different planes in Fig. 1(c). The other process parameters used for producing the bars are illustrated in Table 2. The same process conditions were used to manufacture the billets which were mechanically processed to obtain 26 cylindrical samples having the dimensions illustrated in Fig. 2 according to ASTM E8/E8M-13a standard specification. Due to the cutting, facing and contour turning operations performed on all tensile samples, the

EF was removed and, therefore, all microstructural and pores analyses were related to the CM. For a better understanding of the results, the analyzed tensile samples cross section (Fig. 2) can be considered as the CM_{XZ} (Fig. 1a) thanks to the position of mutual parallelism between the tensile sample axis of symmetry and the xy plane of the build platform (Fig. 1a).

Pores' analysis was performed with a DMi8 Leica[®] optical inverted microscope (OM) equipped with LAS-X 2D image analysis software. All samples were mechanically ground by SiC papers and subsequently polished with colloidal suspension. According to ISO 13322-1:2014, a measurement area has been systematically defined by considering 6 micrographs at a magnification of 100 \times . The relative density was calculated on the same polished surfaces where the Vickers microhardness tests were carried out. Focusing on the tensile samples, it was calculated (Appendix A) on their cross section (Fig. 2). A density of 2.68 $\frac{\text{g}}{\text{cm}^3}$ was considered for AlSi10Mg samples characterized by 0% porosity as reported by Bai et al. (Ref 11).

In the present manuscript, bars were studied in the as-built condition and after different heat treatments. Direct aging was performed at 175, 200 and 225 °C for 6, 8 and 16 h while, for the T6 treatment, bars and billets were solution treated at 505 °C for 4 h, water-quenched and aged at 175 °C for 4 h. The temperature in the electric muffle furnace was controlled by a digital K-type thermocouple in contact with the samples. The microstructure of as-built and heat-treated SL-90 bars was analyzed through optical and scanning electron microscopies (SEM: Nova NanoSEM, FEI Thermo Fisher Scientific, Hillsboro, OR, USA), while the microstructural analysis of the DL-90 bars was omitted according to the study performed in (Ref 5). For a better understanding, SL-90 and DL-90 indicate the single- and double-laser zones (Fig. 1a), respectively, where the bars analyzed in this work were manufactured.

Vickers microhardness profiles were performed both on XZ and XY planes at the top and bottom regions, and distinguishing the CM and EF zones, in the as-built and heat-treated bars. Three microhardness profiles, from the bottom to the top regions, were performed on each XZ plane (EF_{XZ}, CM_{XZ}), each consisting of 54 measures. On the CM_{XY} area, however, ten random measurements were performed. All HV measures were carried out with a load of 500 gf for an indentation time of 15s according to UNI EN ISO 6507. Finally, Vickers microhardness values were also compared to as-built and T6 heat-treated bars printed with a layer thickness of 50 μm analyzed in (Ref 5). Whenever the results of this study are compared to those in (Ref 5), the present samples are referred to as SL-90 (single-laser) and DL-90 (double-laser) while those from (Ref 5) are designated as SL-50 DL-50, referring to their different layer thickness of 90 μm (this work) and 50 μm (Ref 5), respectively.

Tensile tests were performed at room temperature with Z100 Zwick/Roell servo-hydraulic machine according to ASTM E8/E8M-13a standard specification.

Table 1 Chemical composition of SLM ALSI10Mg powder (wt.%)

Al	Si	Fe	Mg	Cu	Mn	Ti	Other
Bal.	10.0	0.12	0.31	0.03	0.005	0.040	< 0.01

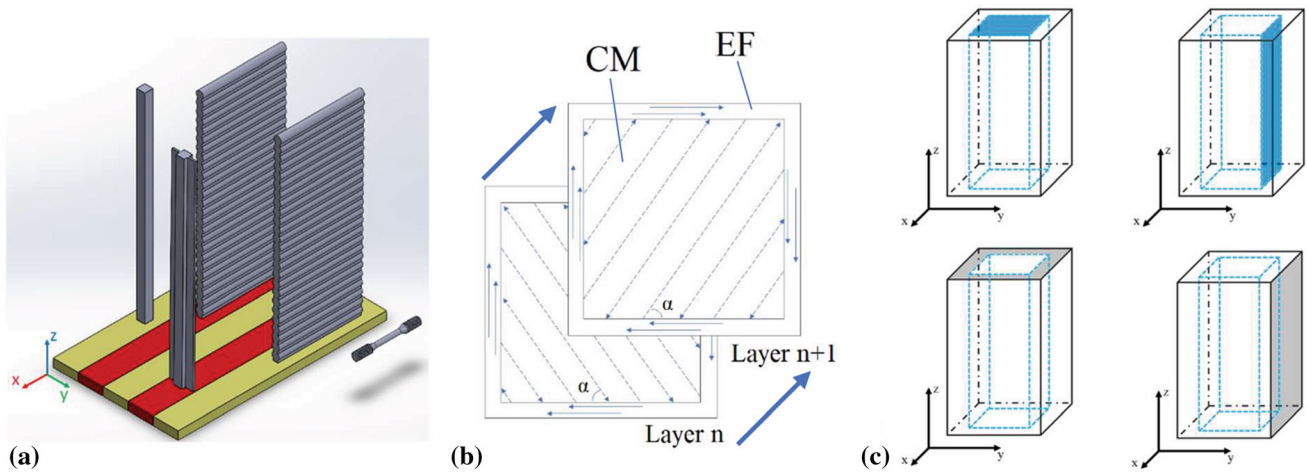


Fig. 1 (a) AlSi10Mg bars ($10 \times 10 \times 300$ mm) printed by a single (blue zones, gray bars) and by double lasers (yellow zone, white bars); (b) scan strategy with $\alpha = 56.5^\circ$ and contour thickness of 200 μ m; (c) graphical representation of different analyzed zones: the CM (light blue) and the EF (gray) (Color figure online)

Table 2 Process parameters used for producing AlSi10Mg bars and billets: external frame (EF) and center zone (CM)

Process parameters	Values for the CM	Values for the EF
Laser power	370W	330W
Scanning speed	1400 $\frac{\text{mm}}{\text{s}}$	600 $\frac{\text{mm}}{\text{s}}$
Layer thickness	90 μm	
Hatch spacing	70 μm	
Pre-heated build platform	150 $^\circ\text{C}$	
Laser beam diameter	100 μm	
Energy density	41.9 $\frac{\text{J}}{\text{mm}^3}$	87.3 $\frac{\text{J}}{\text{mm}^3}$

3. Results and Discussion

3.1 Microstructure and Porosities Before and After Heat Treatments

The as-built microstructure of EF_{XZ} is reported in Fig. 3(a), (b) where the cross section of the laser scan tracks can be observed. Their geometry is conferred by the scan strategy reported in Fig. 1(b).

Focusing on the high magnification micrograph (Fig. 3b) of the EF_{XZ} zone (Fig. 3a), the microstructure shows the presence of columnar grains between two overlapped laser scan tracks, while the equiaxed grains within the layer as discussed in (Ref 18) through the CET (columnar-to-equiaxed transition). Higher-magnification SEM micrographs show (Fig. 3c,d) the α -Al matrix (yellow arrows, panel 1) surrounded by the Si-eutectic particles (yellow arrows, panel 2). Figure 3(d) shows a SEM micrograph emphasizing the cellular structures that are formed during the SLM process of the AlSi10Mg alloy, as also reported by (Ref 19). In Fig. 3(b), it is possible to observe the progressive refinement of the microstructure from the layer boundary to the center due to the heat fluxes generated during the SLM process. In fact, the boundaries of the laser scan tracks

and of the molten pool are characterized by a coarse zone and heat-affected zone (HAZ) (Refs 9, 20).

The high-magnification SEM micrograph shown in Fig. 4 illustrates the Si particles that precipitate within the α -Al matrix due to the L-PBF process (Refs 21, 22). At the same time, their amount increases from the bottom to the top regions due to the pre-heated build platform which influences the Si atoms diffusion from the SSS α -Al (Refs 5, 21, 23). As discussed and analyzed in (Ref 5), the pre-heated build platform induces not only an increase in Si particle amount but also the precipitation phenomena of the ε -Mg₂Si phase (Ref 23).

Figure 5(a) shows a micrograph of the CM_{XY} area showing the laser scan tracks' intersections. It is thus possible to observe different molten pools, characterized by the typical ellipsoidal shape. Their cross sections along the XZ plane are shown in Fig. 5(b) with the yellow dotted lines revealing their boundaries. The same optical micrograph reveals the two typical kind of pores: (1) spherical pores ($< 100 \mu\text{m}$) with a circular geometry; (2) lack-of-fusion pores or LOF ($> 100 \mu\text{m}$) characterized by an irregular shape with their major axis direct on the XY plane (Ref 9). The random pores' distribution, which is predominately formed by spherical pores, is visible in Fig. 5(a), (b) for the CM_{XY}, CM_{XZ} areas and in Fig. 5(c), (d) for EF_{XY}, EF_{XZ} zones, respectively.

Usually, the LOF pores are localized between two adjacent molten pools due to an improper optimization of process parameters, or an inhomogeneous powder bed, or a material discontinuity arising from weak inter-particle bonding (Refs 9, 24, 25).

Spherical pores are instead generated by different gases present within the build chamber or trapped into the gas-atomized powder (e.g., Ar or N) due to its radial pressure distribution within molten Al (Refs 7, 13, 26). On the other hand, hydrogen is the only gas soluble in molten aluminum. Its absorption is caused by the decomposition of moisture in air ($2\text{H}_2\text{O} \rightarrow 2\text{H}_2 + \text{O}_2$) and/or by aluminum oxidation ($3\text{H}_2\text{O} + 2\text{Al} \rightarrow \text{Al}_2\text{O}_3 + \text{H}_2$) as reported by (Ref 27). From an analytical point of view, the hydrogen pores can be formed during the L-PBF process of the AlSi10Mg alloy due to the combination between the short time (t_M) from melting to solidification of the molten pool and the terminal velocity (v_T)

for the pores (Ref 28). These quantities are expressed through Eq. 2 and 3:

$$t_M = l_M/v_s \quad (\text{Eq 2})$$

$$v_T = (2g/9\eta)r_p^2 \quad (\text{Eq 3})$$

where l_M is the molten pool length [m], v_s is the scan speed $\left[\frac{\text{m}}{\text{s}}\right]$, g is the acceleration of gravity $\left[\frac{\text{m}}{\text{s}^2}\right]$, η is the kinematic viscosity [St] of aluminum and r_p is the pore radius [m]. Pores nucleated

at the melting front can escape easier from the pool than those nucleated on the solidification front (Fig. 6) due to the position with respect to the interface between the molten pool and the atmosphere of the build chamber.

Figure 7 shows the microstructure at low magnification after thermal treatments. Figure 7(a)-(c) illustrates the microstructure on the CM_{XY} surface after direct aging for 16 h at 175, 200 and 225 °C, respectively. At the investigated magnification, only for the T6 heat treatment a coarsening of the Si particles is shown in Fig. 7d. This is probably due to the rejection of Si from the

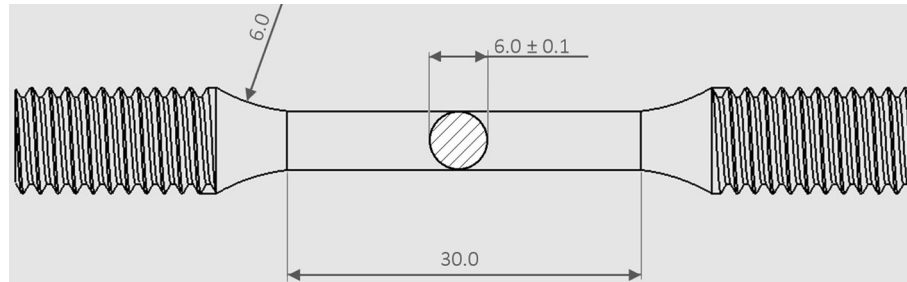


Fig. 2 Graphical representation of a tensile sample obtained through turning operations from the billets. The green arrow indicates the build orientation, while the white circle the tensile sample cross section (Color figure online)

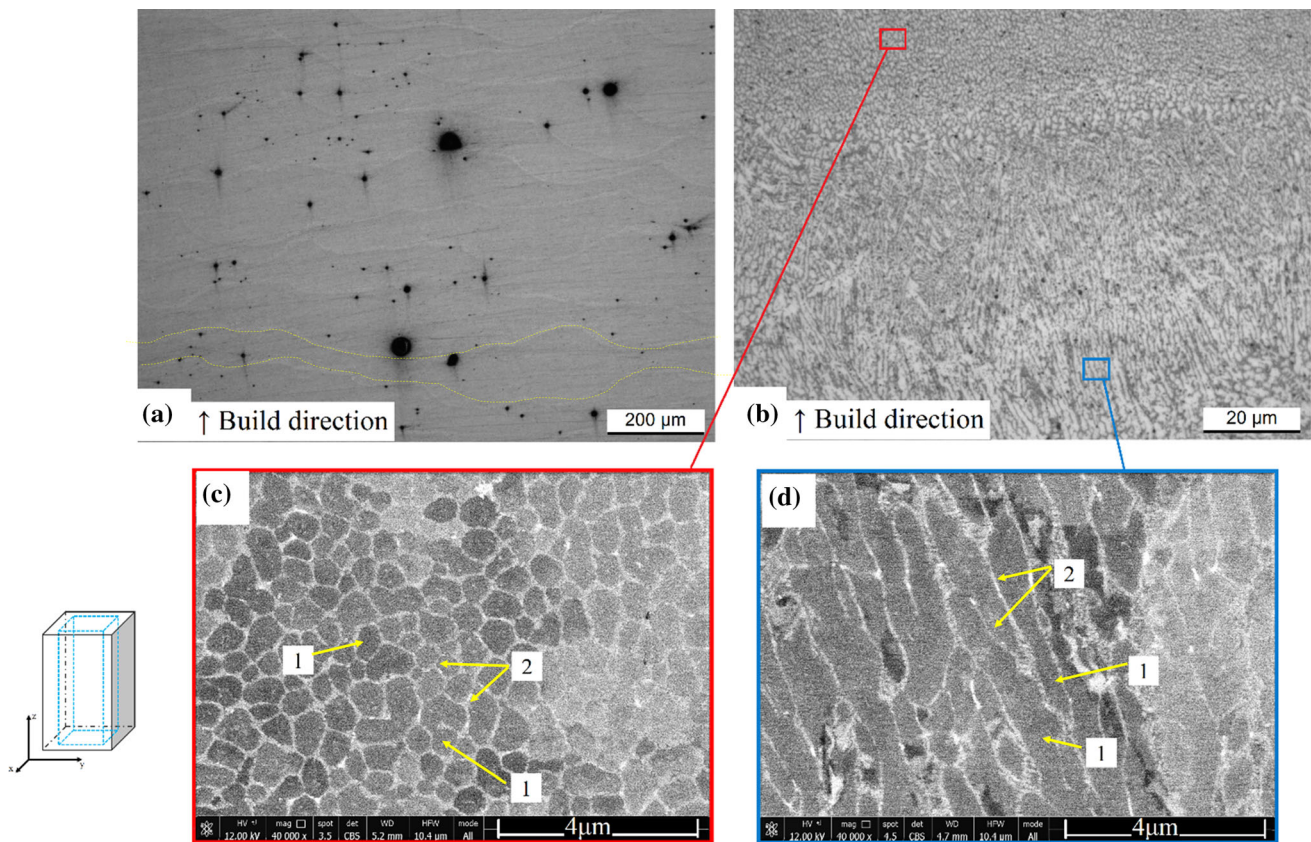


Fig. 3 (a) OM micrograph showing the microstructure of EFXZ in the as-built case. (b) High-magnification micrograph of the microstructure shown in the panel. The dotted yellow lines indicate the boundaries of the scan tracks. The blue and red panels show SEM micrographs of the equiaxed (c) and the columnar (d) grains (Color figure online)

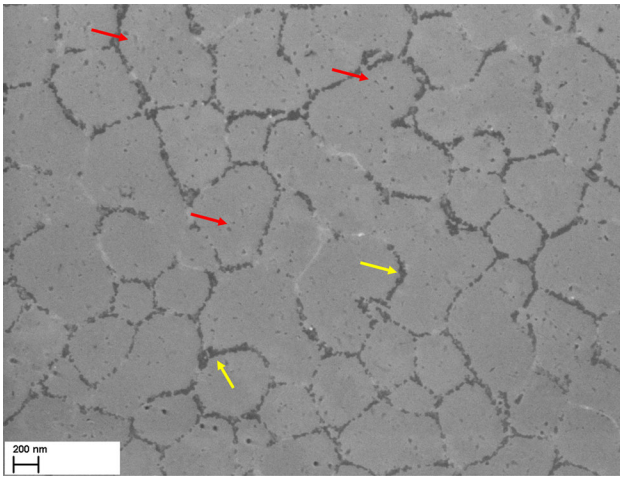


Fig. 4 SEM micrograph of the as-built AlSi10Mg samples where the yellow arrows indicate the Si eutectic network, while the red ones the Si particles that precipitate within the α -Al matrix (Color figure online)

supersaturated α -Al matrix during the SHT (Solution Heat Treatment), as reported by Li et al. (Ref 1). The microstructural configuration that characterizes the L-PBF process remains partially visible even after the T6 heat treatment due to the accumulation of Si particles along the scan tracks or molten pool boundaries rather than at their center (Ref 29) as shown in Fig. 7d. On the other hand, SEM observations illustrate that the eutectic silicon forming the network structure in the as-built samples coarsens at 225 °C, as shown by the comparison of Fig. 8(c) with 8(a) (175 °C-4 h) and Fig. 8(b) (200 °C-6 h). SEM micrographs (Fig. 8d) also confirm the significant microstructural re-arrangement produced by the T6 heat treatment, with much coarser [note the different scale needed in Fig. 8d to visualize the microstructure, compared to Fig. 8(a)-(c)], re-crystallized α -Al grains, identifiable through their channeling contrast. Larger, polygonal Si particles are more randomly distributed and do not form a network surrounding extremely fine, cellular α -Al grains as it happened in the as-built and directly aged samples. Pores (indicated by yellow arrows) and acicular Fe-rich intermetallic (indicated by orange arrows) are also visible in this sample.

The statistical results of image analysis of pores in as-built bars are reported in Fig. 8, for the SL-90 (Fig. 9a,b) and DL-90 samples (Fig. 9c,d) measured in the CM_{XZ} and the EF_{XZ} of the same bar. The analysis was performed at the bottom (Fig. 9a,c) and top regions (Fig. 9b,d) analyzing the relative frequency of the equivalent diameter of the pores (Appendix A). Focusing on the SL-90 case (Fig. 9a,b), the CM_{XZ} surfaces on the bottom and top bars show analogous distributions of equivalent pore diameters ($\leq 25 \mu\text{m}$) with maximum frequency of 10 μm (about 40% of all pores). So, the densities at the bottom and top samples are $99.62 \pm 0.01\%$ ($2.67 \frac{\text{g}}{\text{cm}^3}$) and $99.76 \pm 0.01\%$ ($2.67 \frac{\text{g}}{\text{cm}^3}$), respectively. On the other hand, the EF_{XZ} surfaces are characterized by several pores with a larger diameter (up to 125 μm); it can be emphasized that the statistical distribution of the EF_{XZ} in Fig. 9b shows a homogeneous frequency of pores up to 80 μm . The densities of the bottom and top EF_{XZ} samples are lower than those related to CM_{XZ} surfaces being $97.74 \pm 0.09\%$ ($2.62 \frac{\text{g}}{\text{cm}^3}$) and $97.22 \pm 0.11\%$ ($2.62 \frac{\text{g}}{\text{cm}^3}$), respec-

tively. This slight variation in density between top and bottom regions was obtained due to the almost similar ratio between the total pore area and the total analyzed area ($\sum_{j=1}^6 \hat{A}_j$): 0.023 and 0.028, respectively. In more details, the top region is characterized by higher big pores than the bottom for the fact that the former shows 316 pores with a total area of $6.92 \times 10^5 \mu\text{m}^2$ ($2190.4 \mu\text{m}^2/\text{pore}$) and the latter 630 pores with a total area of $5094 \times 10^5 \mu\text{m}^2$ ($895.4 \mu\text{m}^2/\text{pore}$). In this case, further investigations will be performed to understand what process conditions can influence the difference between these top and bottom regions in terms of pores dimension and quantity. The correlations between the SL-90 machine setup and the energy density values, or between the bar position within the build chamber and the printing process, may be taken as the main causes to analyze. Considering the DL 90 bars, all statistical distributions are narrower and show higher values of relative frequencies (45 ÷ 60% for equivalent diameters of 10 μm) than the SL-90 bars, as also analyzed in Cerri et al. Ref 5. Similar to SL-90 bars, the distribution related to the EF_{XZ} surface reveals the presence of a few very large pores (up to 150 μm) as shown in Fig. 5(d). The densities are $99.20 \pm 0.06\%$ ($2.66 \frac{\text{g}}{\text{cm}^3}$) and $99.33 \pm 0.02\%$ ($2.66 \frac{\text{g}}{\text{cm}^3}$) in the core (i.e., calculated from the CM_{XZ} data) and $86.99 \pm 0.22\%$ ($2.33 \frac{\text{g}}{\text{cm}^3}$) and $95.50 \pm 0.09\%$ ($2.56 \frac{\text{g}}{\text{cm}^3}$) in the skin (i.e., calculated from the EF_{XZ} data). Figure 9(e),(f) shows the statistical distribution of pore sizes on the CM_{XY} surfaces of the SL-90 and DL-90 bars in as-built conditions, comparing the bottom regions (black profile) to the top regions (red profile). In both graphs, a magnification of the equivalent diameter axis was considered comparing Fig. 9(e),(f) with Fig. 9(a)-(c), for the following reasons: (1) the relative frequency tends to zero for sizes higher than 15 μm ; (2) only the shape of the gas pores can be influenced by the low temperature of the pre-heated build platform. In this context, it is possible to observe that the build platform induces a slight difference between the bottom region and the top region in terms of quantity of small pores. In fact, the pores with an equivalent diameter lower than 5 and 7 μm for SL-90 and DL-90 bars, respectively, are characterized by a higher relative frequency considering the top region rather than the bottom region. The same results are obtained by (Ref 13). On the other hand, comparing the results shown in Table 3, the bottom regions are characterized by larger pores than the top regions for all analyzed CM zones.

As noted in Introduction, the energy density values affect the as-built material density more than does the pre-heating temperature of the platform. De facto, plotting the results (Fig. 10) reported by other authors (Ref 9, 11, 23, 30-37) a consistent trend emerges showing very low density (porosity) values at ED lower than 30 ($2.33 \frac{\text{g}}{\text{cm}^3}$), while the maximum ($\sim 2.68 \text{ g/cm}^3$) at energy densities roughly comprised between 35 and 60 ($2.33 \frac{\text{g}}{\text{cm}^3}$), which includes the CM regions from the present work ($35.8 \frac{\text{g}}{\text{cm}^3}$); red points in Fig. 10) and the L-PBFed AlSi10Mg bars analyzed in (Ref 5) ($41.9 \frac{\text{g}}{\text{cm}^3}$, blue point in Fig. 10). The lower density of the EF zones of the SL and DL AlSi10Mg bars studied in this manuscript ($87.3 \frac{\text{g}}{\text{cm}^3}$) is also consistent with the generally decreasing density at the highest energy densities.

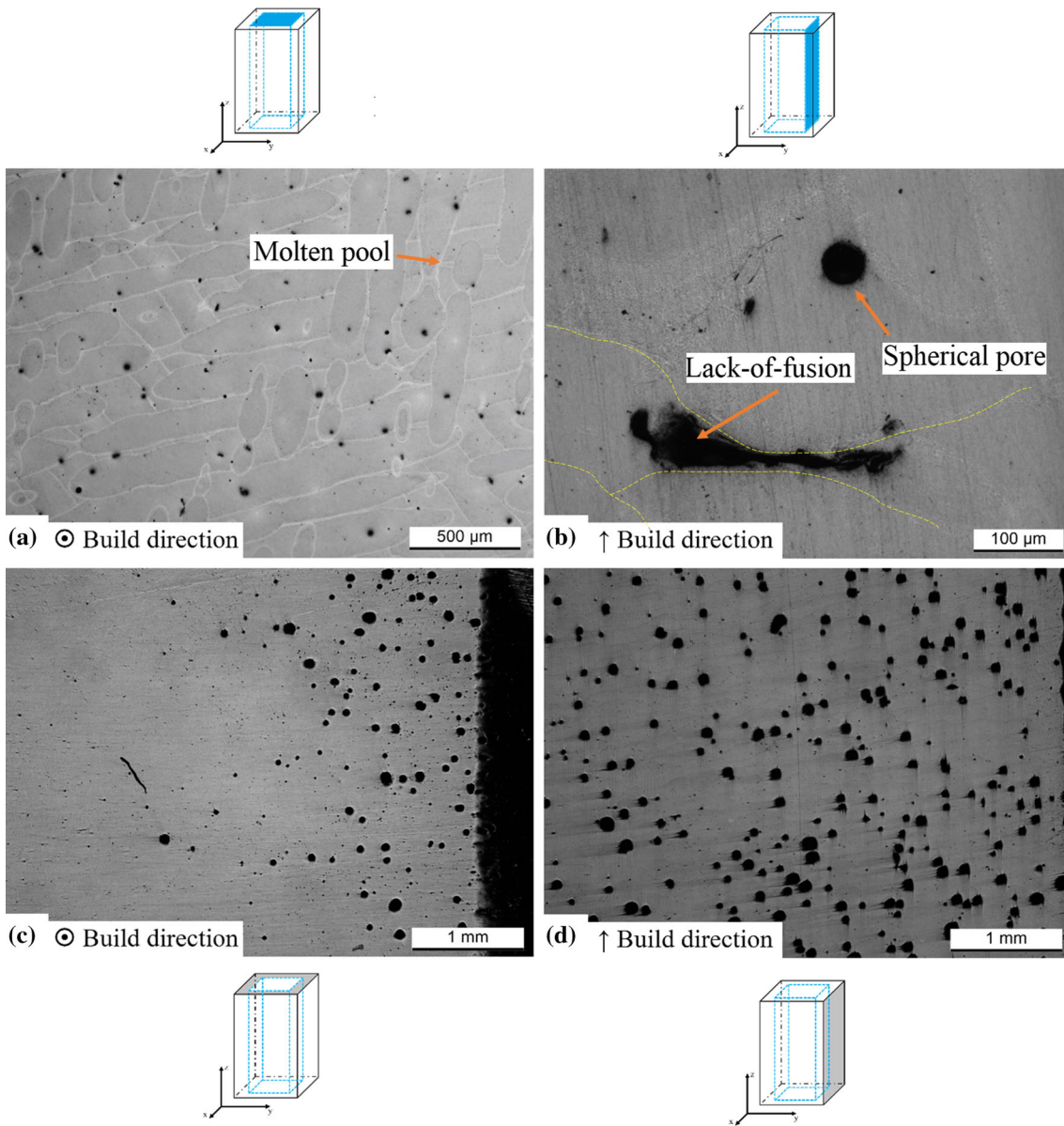


Fig. 5 OM micrographs acquired on CMXY (a), CMXZ (b), EFXY (c) and EFXZ (d). The yellow dotted lines indicate the molten pool boundaries (Color figure online)

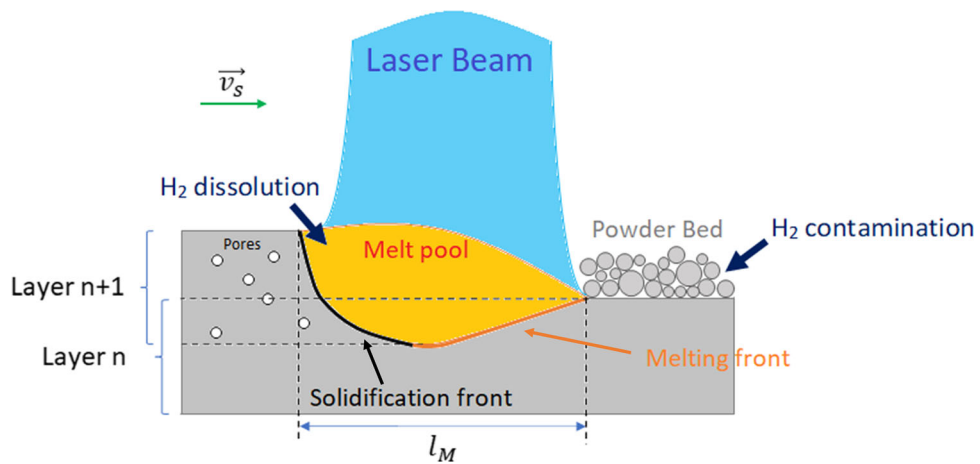


Fig. 6 Schematic representation of gas pores formation during the SLM process

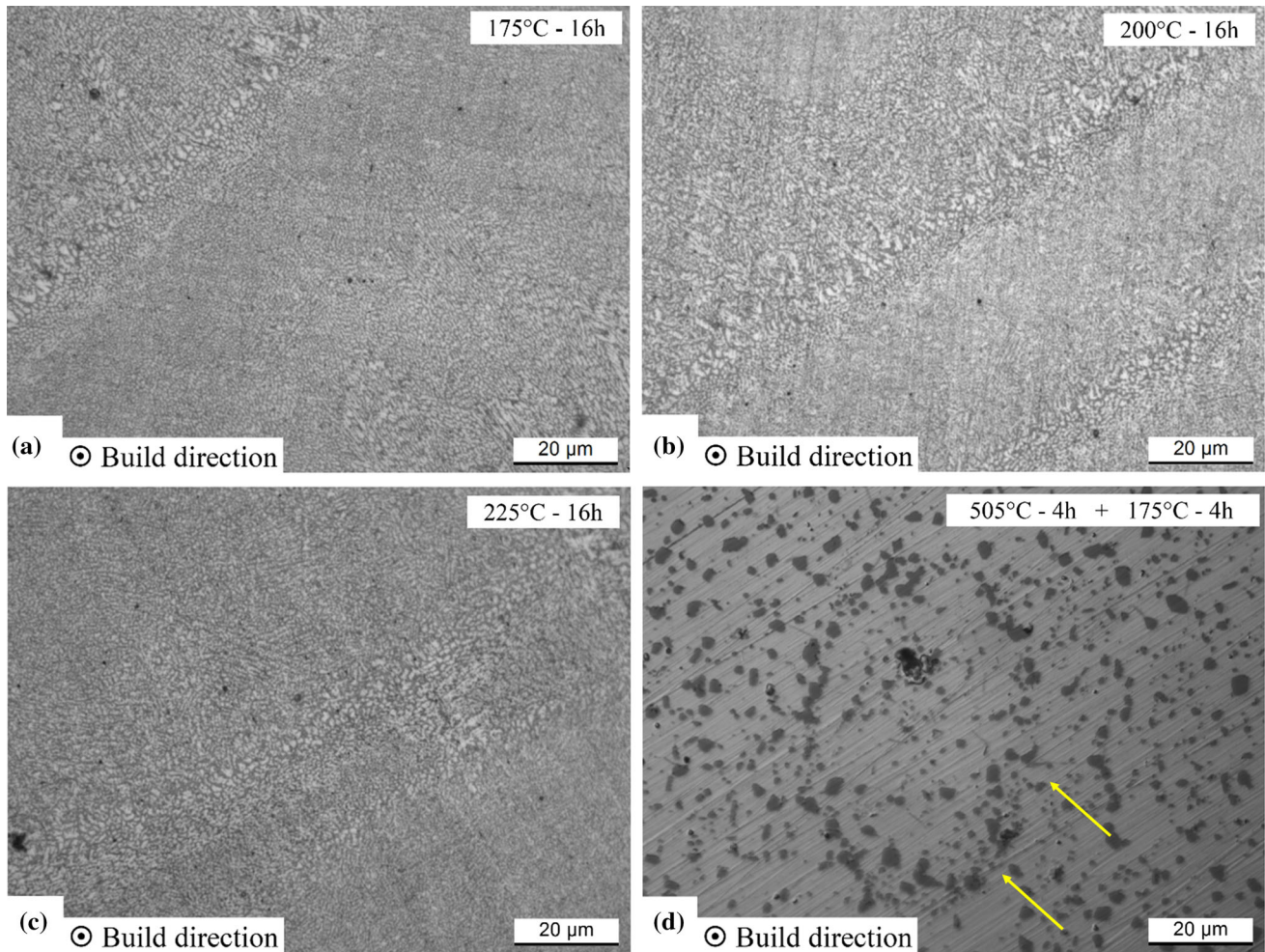


Fig. 7 Microstructure of the CMXY surface of AlSi10Mg bars after direct aging for 16 h at 175 (a), 200 (b) and 225 °C (c), and after the T6 heat treatment (d). The yellow arrows indicate a molten pool that remained visible after the T6 heat treatment

Table 4 reports the density of the AlSi10Mg bars before and after heat treatments. The percentage volume of pores increases with temperature. As a consequence, after the T6 heat treatment the density decreases from 99.87 ± 0.01 to $98.26 \pm 0.08\%$ ($2.63 \frac{\text{g}}{\text{cm}^3}$) and from $99.83 \pm 0.01\%$ to $98.03 \pm 0.02\%$ ($2.63 \frac{\text{g}}{\text{cm}^3}$) at the bottom and top regions, respectively, in the SL-90 bar. The same density (porosity) trend occurs in the DL-90 samples, except for the difference between the bottom ($97.08 \pm 0.12\%$, $2.60 \frac{\text{g}}{\text{cm}^3}$) and the top ($98.07 \pm 0.12\%$, $2.63 \frac{\text{g}}{\text{cm}^3}$) regions.

This trend is also reported by Majeed et al. (Ref 38), who analyzed the influence of T6 and T4 heat treatments on relative density and porosity of SLMed AlSi10Mg samples. Similarly, Girelli et al. (Ref 39) reported that SHTs at 510 and 540 °C reduce the relative density by 1.5 and 3.7%, respectively. Figure 11(a)-(d) illustrates the relationship between the maximum and the minimum dimensions of all pores (Appendix A) analyzed in the present paper (the black and red points are

referred to pores in as-built and T6 heat-treated bars, respectively). Both Fig. 11(a), (b) (SL-90 bars) and Fig. 11(c), (d) (DL-90 bars) show an increase in the aspect ratio (AR) from the as-built to the T6 heat-treated cases (Appendix A). In fact, the red linear fits (T6 samples) shown in Fig. 11 tend to get closer to the blue dashed lines (AR = 1) than the black linear fits (as-built samples).

So, the T6 heat treatment induces a moderate spheroidization of the pores in the SL-90 and DL-90 bars. This is also directly illustrated in Fig. 12, which does confirm a moderate rounding (Appendix A) of some pores (e.g., see the circled pore) when the same area (on the CM_{XY} surface) is imaged in the as-built condition (Fig. 12a) and after the T6 heat treatment (Fig. 12b).

Due to the exposure to the high temperature, the pressure variation at the interface between the gas and the material around it causes a variation in surface energy according to the Young-Laplace equation (Ref 40):

$$\Delta p = \gamma \left(\frac{1}{R_1} + \frac{1}{R_2} \right) \quad (\text{Eq 4})$$

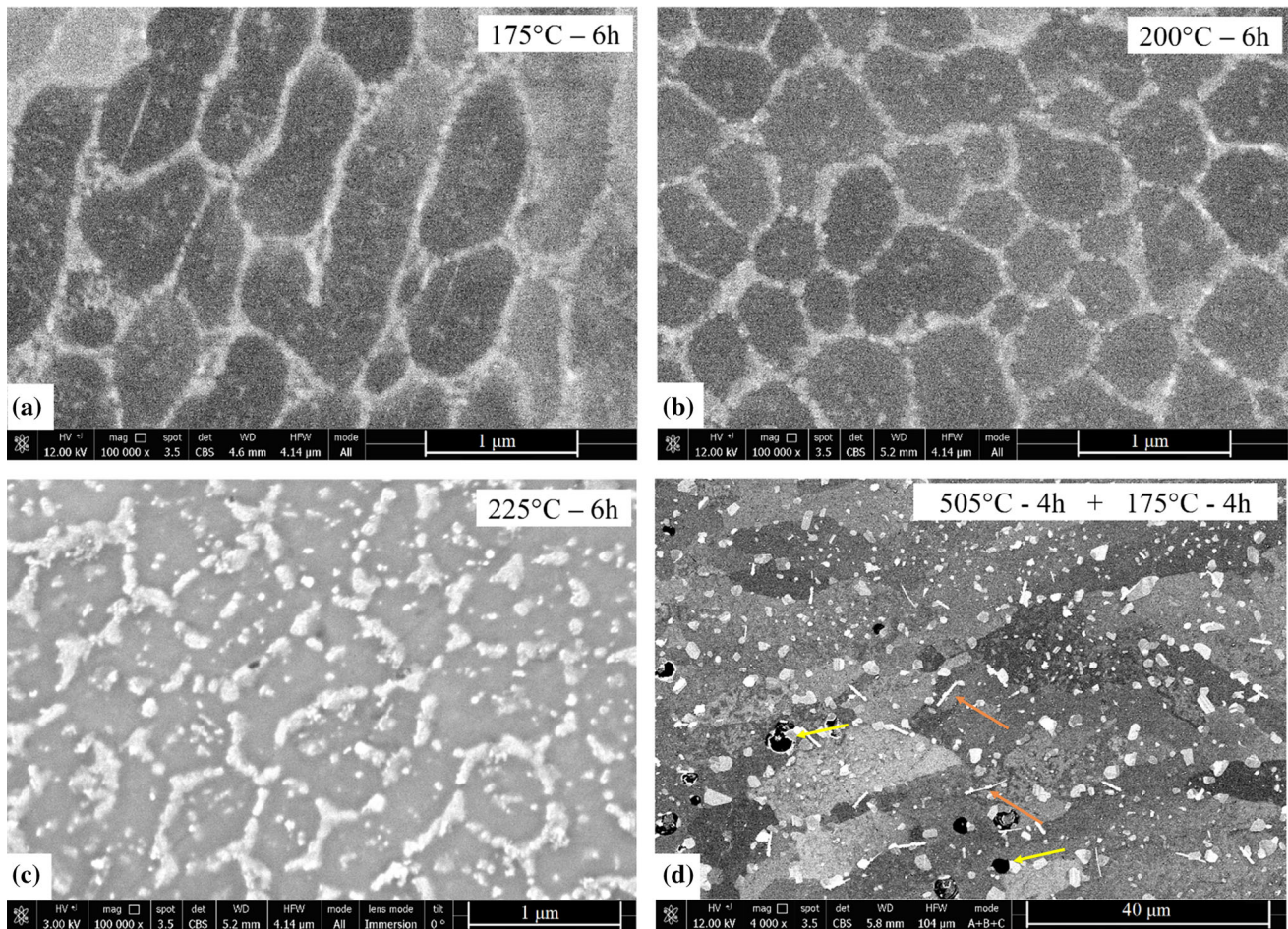


Fig. 8 SEM micrographs of AlSi10Mg microstructure after direct aging for 6 h at 175 (a), 200 (b) and 225 °C (c), and after T6 heat treatment (d)

where Δp is the pressure variation [Pa], γ is the interfacial tension [N/m] and R_1, R_2 are the principal radii of the sharp edges [mm]. Girelli et al. (Ref 39) explain the density variation through the increment of gas pressure within the pores consequently to the increase in temperature. If the temperature is sufficient to reduce the yield strength of the material around the pore, then the gas pressure can deform it. On the other hand, Chaijaruwanich et al. (Ref 41) suggested the activation of inter-pores Ostwald ripening. Gu et al. (Ref 42) show the same tendency to reduce the pore surface energy after the solution heat treatments in the range between 530 and 540 °C. Finally, the same authors (Ref 42) show the formation of small new pores during the T6 heat treatment as also shown in Fig. 12 (the arrow points out to a small pore formed after the T6 treatment, panel b, at a location where none was present in as-built condition, panel a).

Figure 13 reports the roundness and the maximum dimension (length) of all analyzed pores, before (Fig. 13a) and after the T6 heat treatment (Fig. 13b). As previously reported, gas and LOF pores are characterized by a spherical shape with smaller ($< 100 \mu\text{m}$) size, and an irregular shape with bigger ($> 100 \mu\text{m}$) size, respectively. The orange (roundness > 0.5 ,

length $< 100 \mu\text{m}$) and the yellow (roundness < 0.5 , length $> 100 \mu\text{m}$) regions in Fig. 13 represent these different kinds of porosity. According to Fig. 13(a) where 99.9% of pores represent the spherical pores, the bars are characterized by a greater quantity of gas pores than LOF pores confirming the discussion about the graphs shown in Fig. 8(e), (f). After the T6 heat treatment (Fig. 13b), the pores' population piled even more toward roundness values close to 1. Accordingly, changes to the pores' distribution after the T6 heat treatment mainly concerned the pores with an equivalent diameter $< 20 \mu\text{m}$, as shown in Fig. 14(a). The red profile (T6 heat treatment) has lower relative frequencies for small pores ($< 10 \mu\text{m}$) than the black one (as-built) and higher relative frequencies for pores with an equivalent diameter $> 10 \mu\text{m}$. The density variation after the T6 heat treatment can be caused by the previously discussed phenomena (Refs 39, 40, 42). In addition, this variation can also occur due to the microstructural variation taking place during the SHT (Fig. 8) and due to the precipitation phenomena induced by the artificial aging (Refs 38, 43). Figure 14(b) shows the same results obtained after the analysis of the tensile samples cross section before and after the T6 heat treatment.

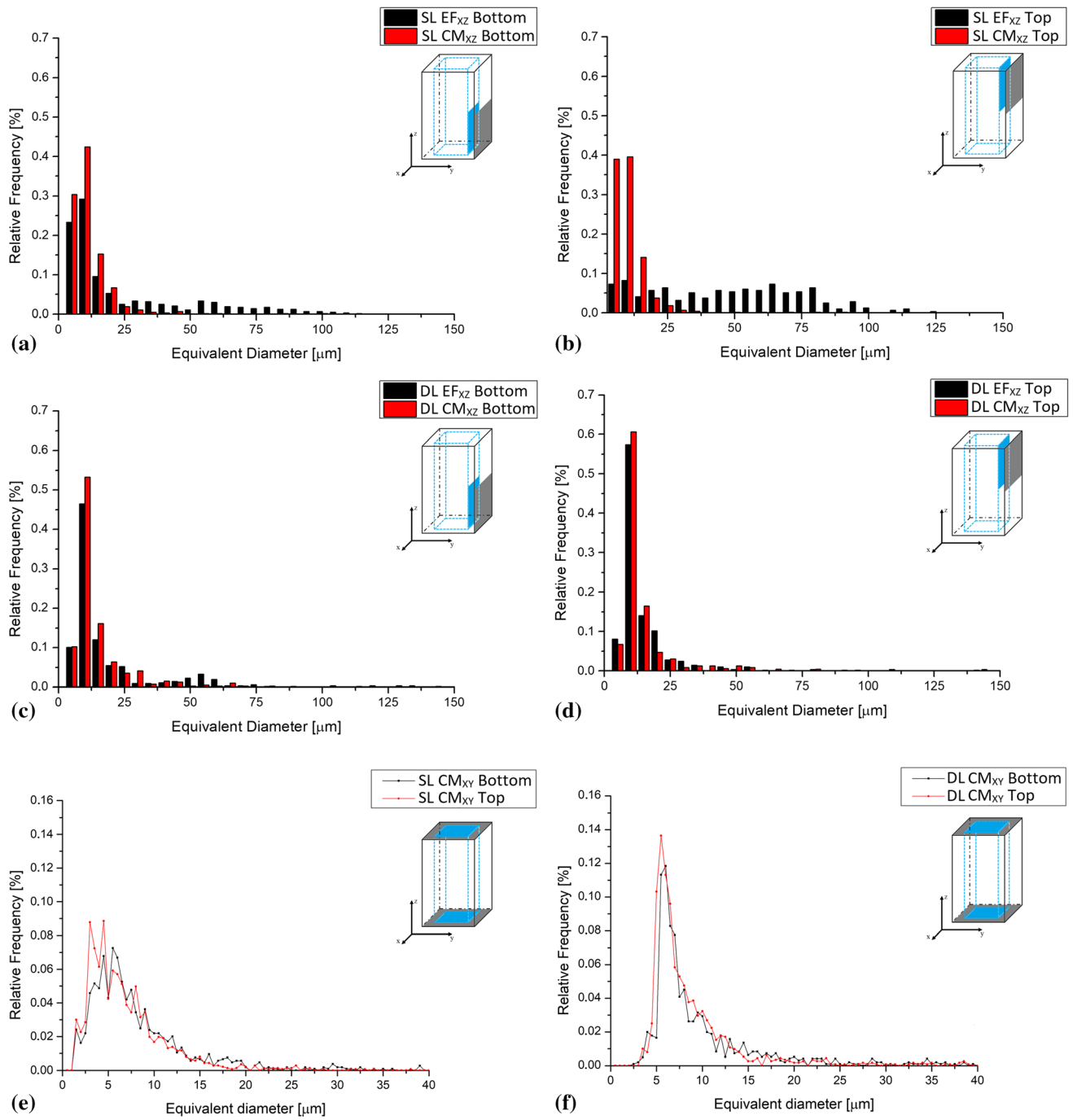


Fig. 9 Statistical distribution of porosity for SL-90 (a, b, e) and DL-90 (c, d, f) samples analyzed along EFXZ, CMXZ and CMXY of the bars. The graphs (a, c) and (b, d) are referred to the bottom and top regions, respectively. (e, f) compare the bottom region to the top region

Table 3 Averaged values of the area per pore ($\mu\text{m}^2/\text{pore}$)

	Bottom		Top	
	CM _{XZ}	CM _{XY}	CM _{XZ}	CM _{XY}
SL-90	149 ± 6	100 ± 3	85 ± 3	64 ± 3
DL-90	645 ± 25	640 ± 25	293 ± 12	246 ± 10

3.2 Analysis of Vickers Microhardness and Mechanical Properties

Figure 15(a), (b) shows the Vickers microhardness profile (columns) of the bars along the build direction, over their entire 300 mm length, together with the trends of density values (dashed-dotted lines) according to Table 3, for the SL-90 (Fig. 15a) and DL-90 as-built bars (Fig. 15b).

Figure 15(a) shows that, going from the bottom surface of

the bar ($z = 0$) to the top surface ($z = 300$ mm), HV profiles measured along the z -axis exhibit a decreasing trend in both CM_{XZ} and EF_{XZ} planes, while the density values remain constant at 2.68 and $2.62 \frac{g}{cm^3}$, respectively. So, it is reasonable to assume that the decrease in HV depends on aging induced, in the L-PBFed AlSi10Mg bars, by the temperature of the SLM building platform, set at 150 °C. At this temperature, the Si- and Mg-supersaturated Al matrix gives rise to the precipitation of very fine Si and Mg_2Si particles as illustrated in Fig. 4 (Ref 5). Precipitation hardening is stronger at the bottom of the bar than at the height of 300 mm due to the longer exposure time of the bottom region during the SLM process. The same decreasing trend of the SL EF_{XZ} profile along the z -axis is also found in SL CM_{XZ} values. The latter are approximately 10 HV higher due to the higher density in the CM region (a difference of $0.06 \frac{g}{cm^3}$). A decreasing trend is analogously

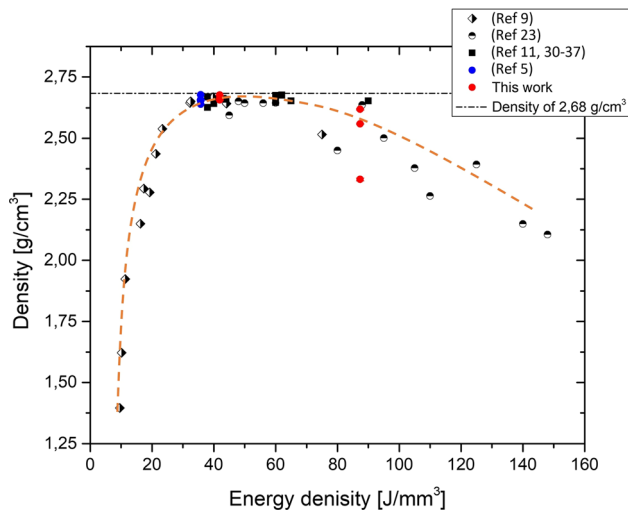


Fig. 10 Density values as a function of energy density obtained in the present study and reported in (Refs 5, 9, 11, 30-37)

found in Fig. 15(b) for the DL bar on both EF_{XZ} and CM_{XZ} surfaces, again due to aging effects. Notably, the HV profile on the DL EF_{XZ} surface shows a plateau in the bottom region, unlike all other measurements. This is probably due to the higher porosity: indeed, density changes by about $0.33 \frac{g}{cm^3}$ between the CM_{XZ} ($2.66 \frac{g}{cm^3}$) and the EF_{XZ} zones ($2.33 \frac{g}{cm^3}$). The material is obviously weakened by higher porosity, counteracting the aging effects generated by the pre-heated build platform: the porous material indeed tends to collapse under the load transmitted by the pyramidal diamond Vickers indenter as reported by Tiwari et al. (Ref 14).

Figure 14(c) shows the Vickers microhardness profile measured on the XY plane (perpendicular to the build direction) of SL-90 bottom (orange columns) and top (brown columns) samples before and after the heat treatments. In the as-built conditions, the hardness difference between bottom and top samples is confirmed. After aging at 175 °C for 8h, the hardness of the top samples increases (from 115 ± 5 HV to 132 ± 2 HV) due to precipitation phenomena, as demonstrated by Casati et al. (Ref 24) through DSC analysis. The bottom samples, on the other hand, might have faced an overaging process, and their microhardness decreases from 132 ± 3 to 127 ± 1 HV. As a result, the microhardness difference between the two regions is largely levelled out. After 16 h at 175 °C, HV values between top and bottom samples are fully homogenized, and the same is true for all the other direct aging heat treatments performed. The decreasing trend of the HV values with increasing treatment temperature is a combined effects of microstructural coarsening (Fig. 8) and density variation (Ref 5).

The lowest HV values are found in the T6 samples, due to the complete microstructural change as reported in Fig. 8 as well as the increased porosity, as shown by the dashed curves. Whereas, however, the microstructural configuration of the bottom and top regions is completely homogenized after the T6 heat treatment, the ΔHV between the bottom and top regions (Table 5, 6, Fig. 15) is caused by the variation in density. For example, considering the DL bar (orange and yellow columns),

Table 4 Density values of SL and DL AlSi10Mg bars before and after heat treatments along the build direction and XY plane. The results from this work are also compared to the SL-50 and DL-50 samples previously characterized in (Ref 5)

Planes	HT conditions	SL		DL	
		Bottom, %	Top, %	Bottom, %	Top, %
CM_{XY-90}	As-built	99.87 ± 0.01	99.83 ± 0.01	99.15 ± 0.03	99.36 ± 0.02
	175 °C/8 h	99.81 ± 0.02	99.64 ± 0.02
	175 °C/16 h	99.72 ± 0.01	99.78 ± 0.01
	200 °C/8 h	99.73 ± 0.02	99.60 ± 0.02
	200 °C/16 h	99.67 ± 0.02	99.66 ± 0.01
	225 °C/8 h	99.29 ± 0.02	99.29 ± 0.02
	225 °C/16 h	98.92 ± 0.02	99.19 ± 0.02
CM_{XZ-90}	T6	98.26 ± 0.08	98.03 ± 0.02	97.08 ± 0.12	98.07 ± 0.02
	As-built	99.62 ± 0.01	99.76 ± 0.01	99.20 ± 0.05	99.33 ± 0.02
CM_{XZ-50} (Ref 5)	T6	98.15 ± 0.06	97.95 ± 0.04	97.58 ± 0.10	98.12 ± 0.08
	As-built	99.00 ± 0.01	98.5 ± 0.03	99.9 ± 0.01	99.2 ± 0.05
EF_{XZ-90}	As-built	97.74 ± 0.09	97.72 ± 0.11	86.99 ± 0.22	95.50 ± 0.09

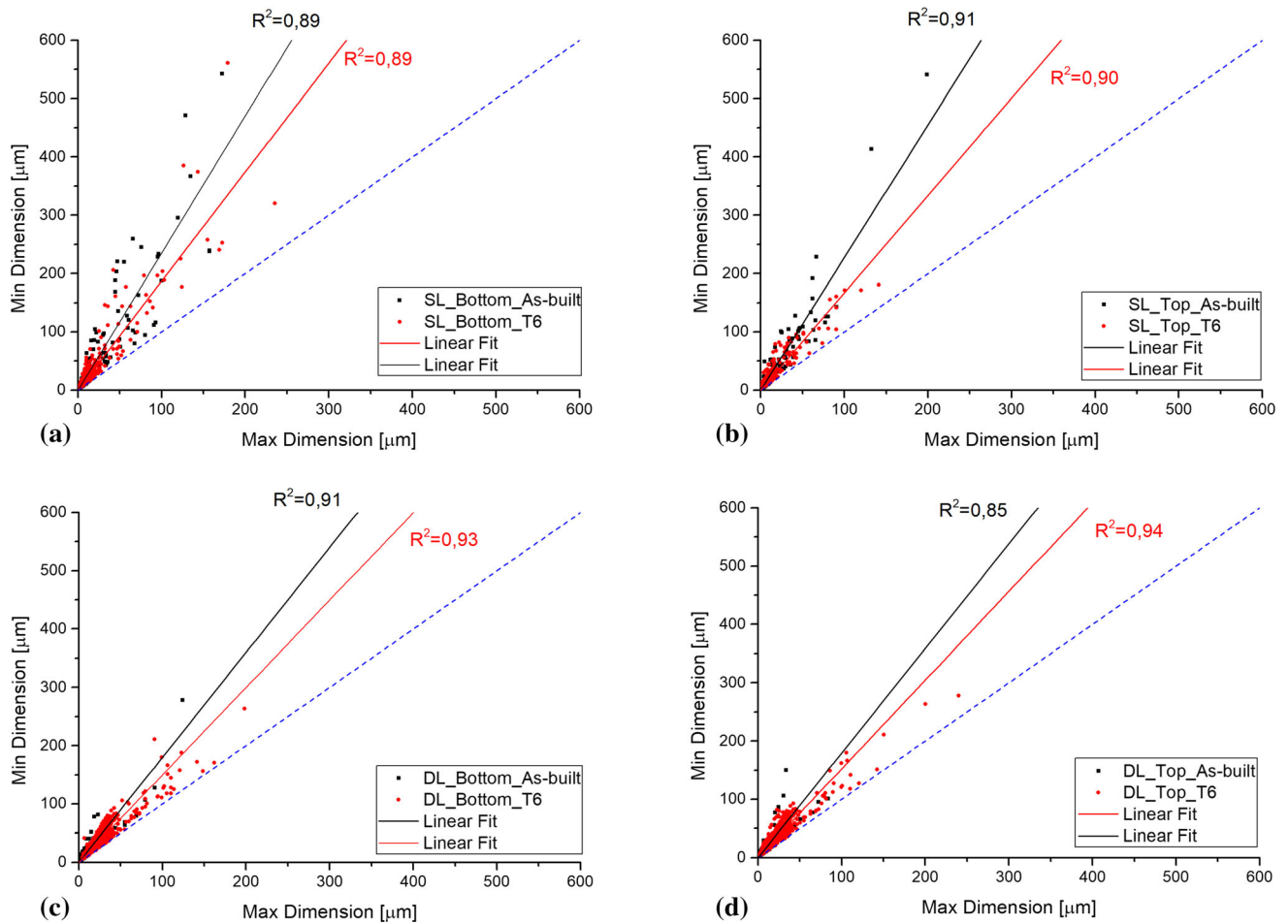


Fig. 11 Graphs show the maximum and minimum dimension of all pores analyzed before and after the T6 heat treatment for SL-90 (a, b) and DL-90 (c, d) bars. The dashed blue line represents the pore's aspect ratio equal to 1 (Color figure online)

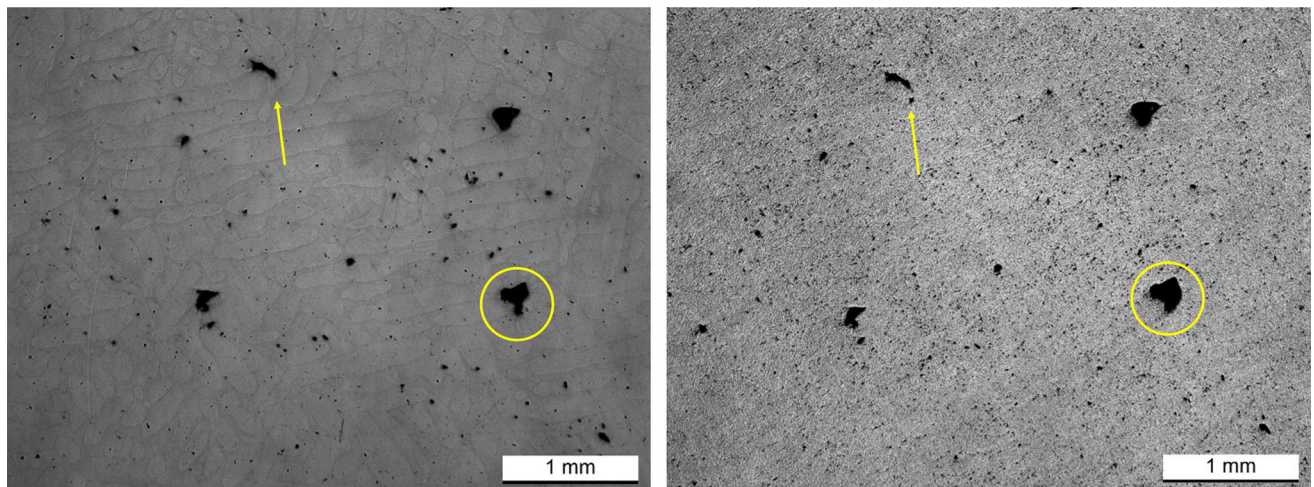


Fig. 12 OM micrographs acquired at the same location on the CMXY surface before and after the T6 heat Treatment

the variation between bottom region (81 ± 2 HV) and the top region (86 ± 1 HV) is accompanied by a density variation of + 1%. The same results are obtained with the SL-50 and the DL-50 AlSi10Mg bars analyzed in Cerri et al. (Ref 5). The Δ HV between the top and bottom regions is confirmed by the

mechanical properties variation in terms of ultimate tensile strength and yield strength as analyzed in (Ref 18).

The Vickers microhardness is directly correlated with and affected by the porosity (Ref 44) as illustrated in Fig. 16(a), where the effect of density on HV values is reported. In this graph, HV and density values analyzed in the present manu-

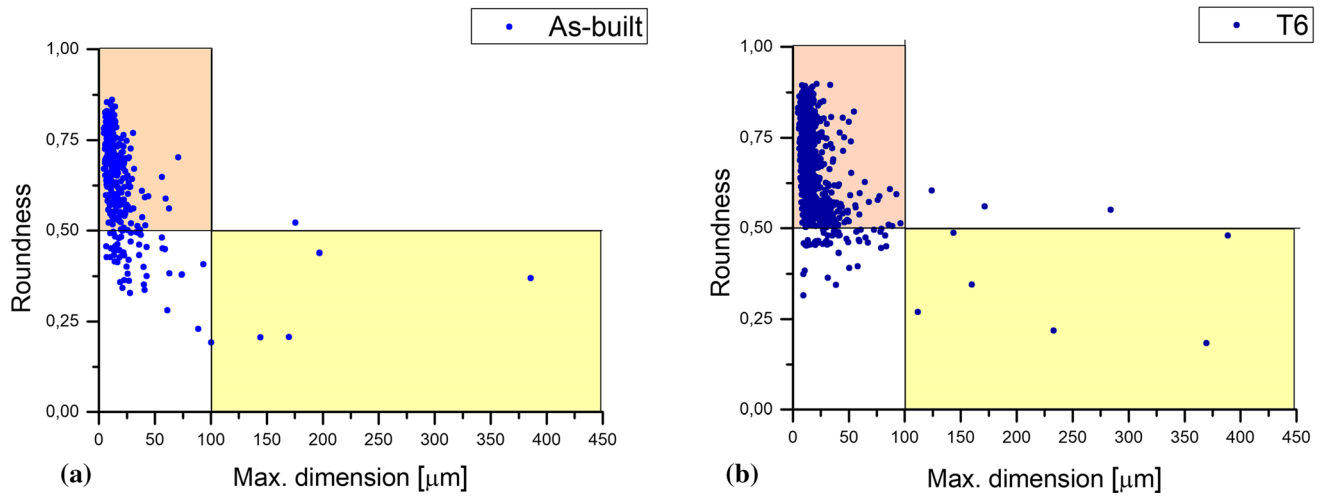


Fig. 13 Roundness and maximum dimension (length) of pores analyzed on the AlSi10Mg samples (XZ plane) in as-built condition and after the T6 heat treatment

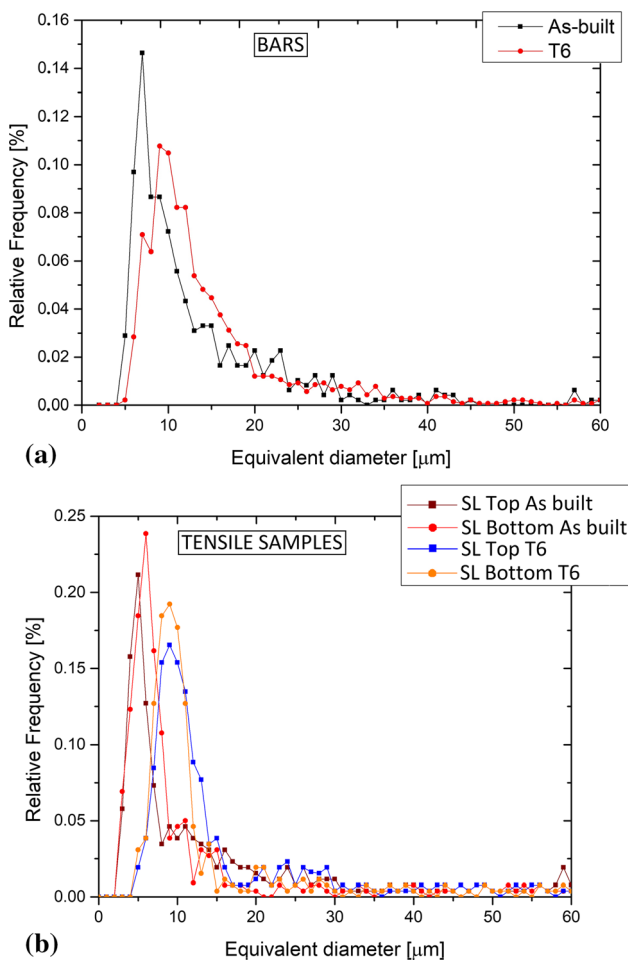


Fig. 14 Statistical distribution of pores before and after T6 heat treatment related to the bars (a) and tensile samples (b)

script (orange, red and white symbols) were compared to those obtained in the literature (black square symbols) and (Ref 45). Focusing on the same graph, the HV values related to the top regions of the as-built bars (orange symbols) show a behavior fully comparable to that reported by (Ref 45). Instead, the HV values associated with the bottom regions (red symbols) show higher microhardness values than those reported by (Ref 45) for the same densities, due to the higher permanence time on the build platform pre-heated at 150 °C than it occurred with the cubic samples in (Ref 45). Finally, the T6 heat-treated bars show the same trend, namely a decrease in microhardness with decreasing density, but the curve is almost rigidly shifted toward lower HV values due to the microstructural changes as previously discussed (Section 3.1).

The correlation between the variation in density ($\Delta\rho$) and the microhardness variation (ΔHV) is also analyzed considering the same regions in as-built condition and after the heat treatment. This experimental procedure nullifies the microstructural and precipitation contributions on the Vickers microhardness.

Through the results obtained in this work (black symbols), the microhardness variation becomes larger as the increase in density grows larger, too. The largest density variations ($0.25 \frac{g}{cm^3} \div 0.35 \frac{g}{cm^3}$), which are highlighted through the dotted yellow ellipse, were obtained considering the density values of the EF_{XZ} , CM_{XZ} and CM_{XY} bottom zones of the DL bar. In fact, as previously discussed through Fig. 4 and Table 3, the high $\Delta\rho$ between these zones causes a strong decrease in the hardening effects induced by the precipitation phenomena.

The changes in Vickers microhardness were correlated with the density variation through a linear fit (Eq 5) and a second-order polynomial fit (Eq 6):

$$\Delta\rho = 17.94\Delta HV - 18.58 \quad (\text{Eq 5})$$

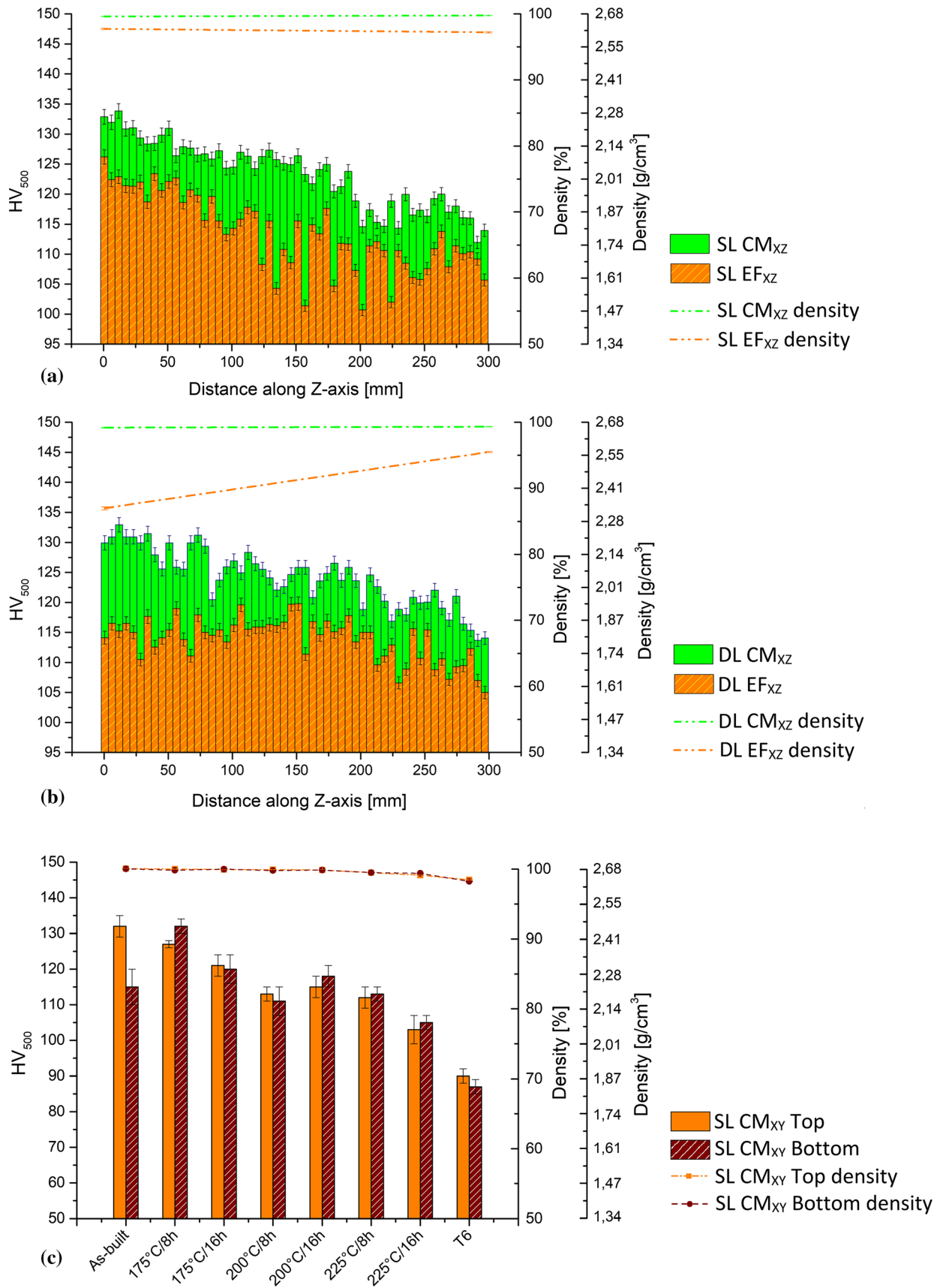


Fig. 15 Vickers microhardness profiles of as-built SL (a) and DL (b) AlSi10Mg bars performed along the EFXZ (orange columns) and the CMXZ (green columns) surfaces. Vickers microhardness values of SL-90 AlSi10Mg bars measured on the XY plane before and after the T6 heat treatment. The dashed lines are referred to the density values

Table 5 Vickers microhardness and density values of the as-built and T6 AlSi10Mg bars

AlSi10Mg bars	As-built		T6	
	HV	Density, %	HV	Density
<i>SL-90</i>				
Bottom	129 ± 3	99.87 ± 0.01	90 ± 2	98.26 ± 0.02
Top	122 ± 4	99.83 ± 0.03	88 ± 3	98.03 ± 0.01
<i>SL-50 (Ref 5)</i>				
Bottom	128 ± 3	99.00 ± 0.02	81 ± 2	97.17 ± 0.03
Top	121 ± 4	98.50 ± 0.04	95 ± 2	98.06 ± 0.02
<i>DL-90</i>				
Bottom	115 ± 5	99.15 ± 0.02	87 ± 2	96.30 ± 0.01
Top	110 ± 3	98.07 ± 0.06	93 ± 3	97.20 ± 0.03
<i>DL-50 (Ref 5)</i>				
Bottom	110 ± 2	99.90 ± 0.01	86 ± 1	98.03 ± 0.02
Top	111 ± 5	99.2 ± 0.02	91 ± 2	97.08 ± 0.01

The results from this work are related to those obtained in (Ref 5)

Table 6 Standard errors associated with the pore area

Areas	Standard error, %
1 $A_p < 1 \mu\text{m}^2$	10
2 $1 \mu\text{m}^2 \leq A_p < 10 \mu\text{m}^2$	7
3 $10 \mu\text{m}^2 \leq A_p < 30 \mu\text{m}^2$	6
4 $A_p \geq 30 \mu\text{m}^2$	4

$$\Delta\rho' = 1.45\Delta\text{HV}^2 - 2.29\Delta\text{HV} + 15.43 \quad (\text{Eq 6})$$

The second-order polynomial fit (blue curve in Fig. 16b Adjusted $R^2 = 0.90$) provides a better match to the data than the linear fit (red line-Adjusted $R^2 = 0.77$). In Fig. 16(b), the ΔHV and the $\Delta\rho$ values obtained from the results shown and discussed in (Ref 44) were plotted through the green symbols: their trend is also consistent with the polynomial fit. Moreover, it is possible to conclude that, even with different L-PBF process parameters and different heat treatment conditions employed in (Ref 44), the correlation between changes in Vickers microhardness and changes in sample density was unaffected.

Figure 17 illustrates the mechanical properties of the as-built and T6 AlSi10Mg tensile samples in relation to the distance from the build platform. As previously discussed for the HV values (Fig. 14a,b), also the UTS and YS values are characterized by decreasing trends from 0 to 300 mm due to the precipitation phenomena. The ductility values, instead, do not show the same trend most likely because the Si-eutectic network, which dominated the fracture mechanism of the as-built samples, does not vary from bottom to top regions (Ref 5, 19, 46-48). At the same time, the pores can be considered as a secondary contribution on the fracture mechanism due to the high-density values of the tensile test samples cross section (Table 4) (Ref 49, 50). After the T6 heat treatment, the UTS and

YS values were homogenized between the bottom and top regions due to the microstructural variation obtained after the SHT (Fig. 7, 8). As concern the elongation values, which were analyzed in (Ref 19), part of the T6 heat-treated samples is characterized by a ductile fracture (also reaching 15%), while another by a more fragile behavior (reaching 7 ÷ 9%). Also in this scenario, the elongation values may be not significantly affected by the pores thanks to the high values shown in Table 5.

4. Conclusions

The present paper studied the porosity in a laser powder bed-fused Al-Si-Mg alloy and its relation to Vickers microhardness and mechanical properties. Direct aging and T6 heat treatments were also analyzed in terms of their effects on microstructure, pores and Vickers microhardness. Only the mechanical properties of the as-built and T6 heat-treated samples were discussed due to their high-density values characterizing the CM of the direct aging samples. The following conclusions could be determined:

- (1) Lack-of-fusion pores ($> 100 \mu\text{m}$, roundness < 0.5) and spherical pores ($< 100 \mu\text{m}$, roundness > 0.5) were found in all samples; but only the 0.01% of all pores consists of LOF pores.
- (2) As the build platform was pre-heated to 150 °C, the bottom regions of the CM zones are characterized by larger pores than the top regions. However, the greatest differences in density can be attributable to the energy density variation from 41.9 to 87.3 $\frac{\text{J}}{\text{mm}^3}$ between the center (CM) and external frame (EF) of the samples, respectively.
- (3) The as-built bars are always characterized by a decrease in microhardness values along the total height (300 mm) in both CM and EF regions, due to the aging phenomena induced by the pre-heated build platform in the bottom region. In the bars built with a dual-laser scan, high porosity in the bottom layer ($\Delta\rho \approx 0.3 \frac{\text{g}}{\text{cm}^3}$ between the bottom and the top parts of the bar) partially offsets the effects of aging. The same decreasing trend was observed even for the mechanical properties for both the single and dual laser. In these cases, the amount of small pores and the high-density values do not take part significantly on ductility variation.
- (4) The T6 heat treatment induces moderate spheroidization and coalescence of the smallest pores ($< 15 \div 20 \mu\text{m}$), as well as the formation of new pores. The complete destruction of the cellular structure that characterized the as-built and directly aged bars and the reduction in density caused a remarkable decrease ($- 30\%$) of the Vickers microhardness in the T6 samples. This microstructural variation removes the effects induced by the pre-heated build platform.
- (5) Considering all samples in both as-built and heat-treated conditions, the best fit between the relative density and microhardness variations is $\Delta\rho' = 1.45\Delta\text{HV}^2 - 2.29\Delta\text{HV} + 15.43$.

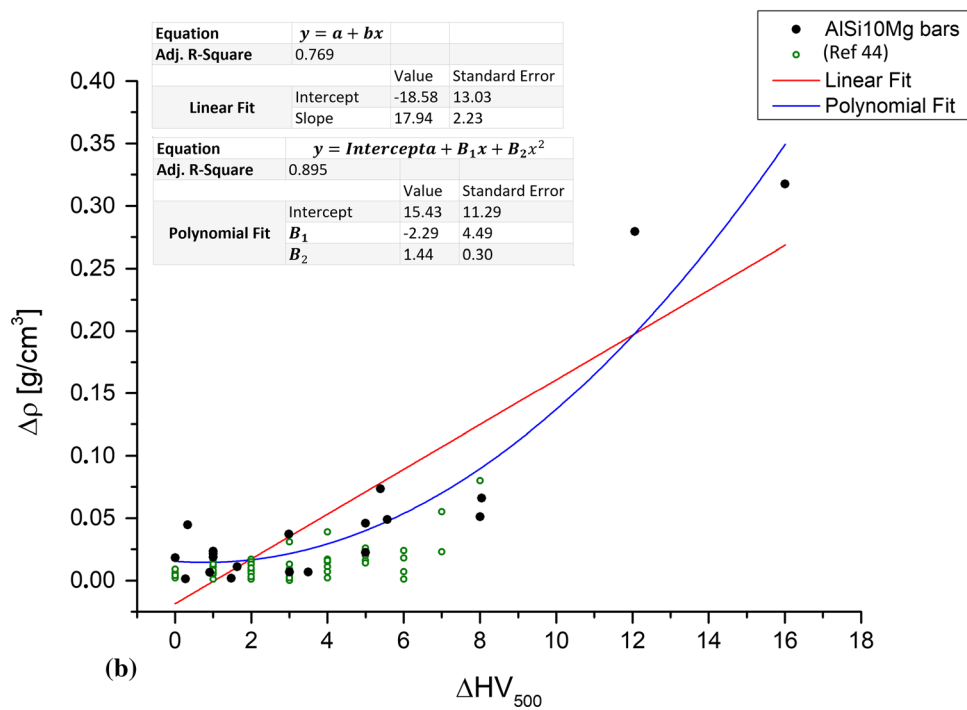
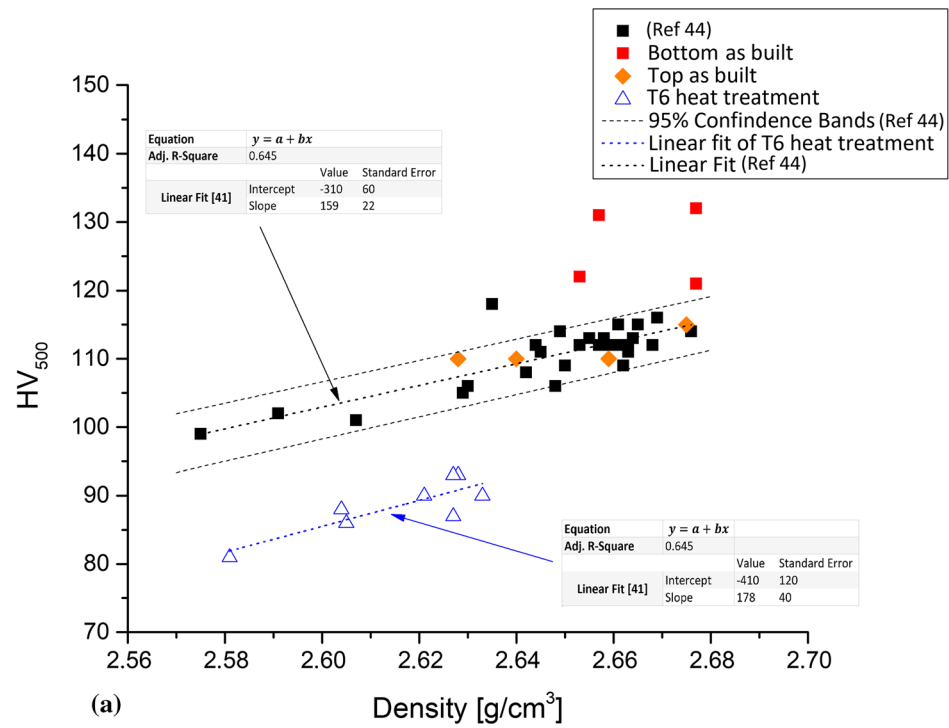


Fig. 16 (a) Effect of density on Vickers microhardness, (b) linear and polynomial fits between the microhardness variations and the density variation

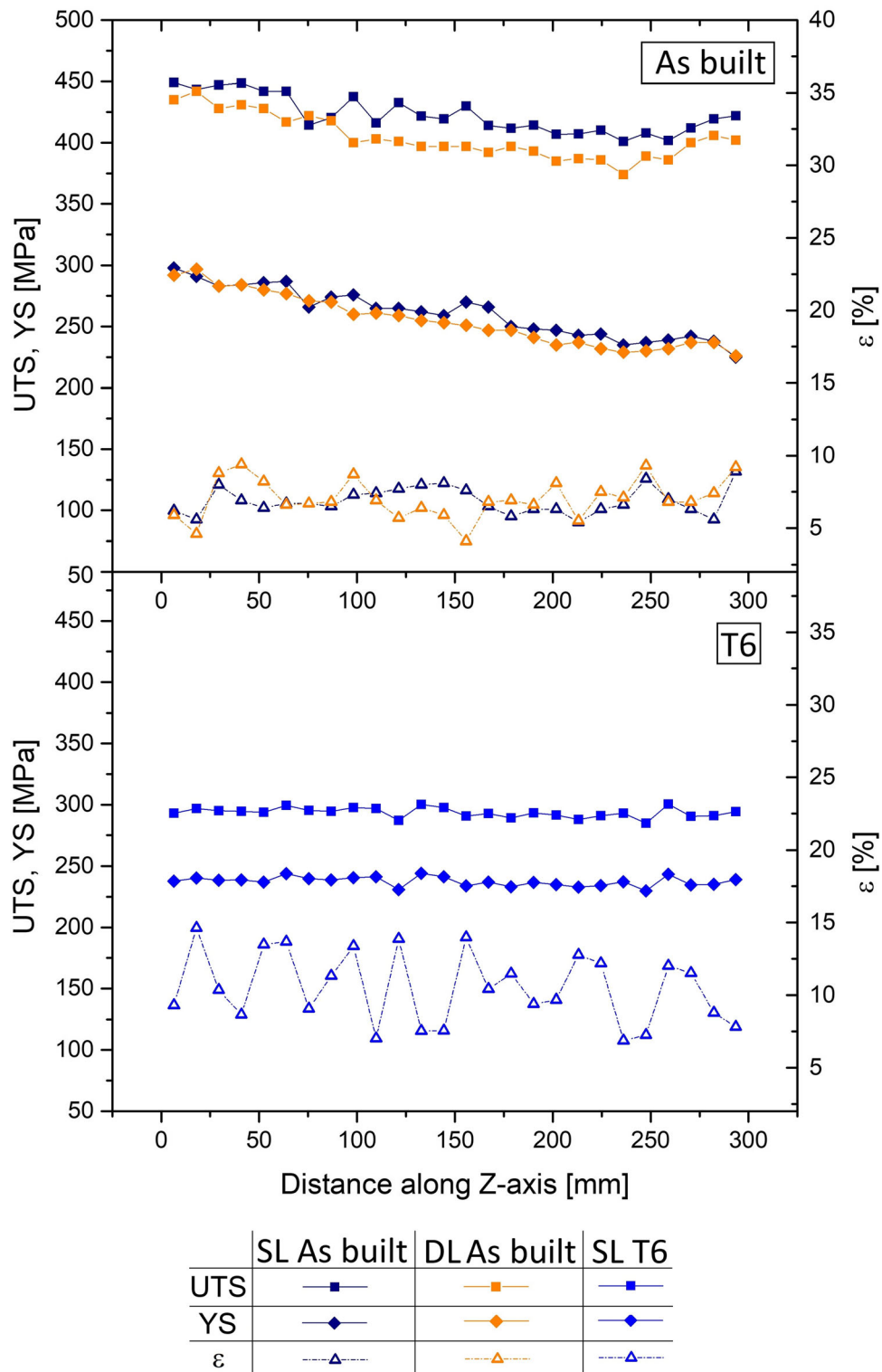


Fig. 17 Tensile properties of the SL-90 and DL-90 as-built samples and of the T6 SL-90 AlSi10Mg samples

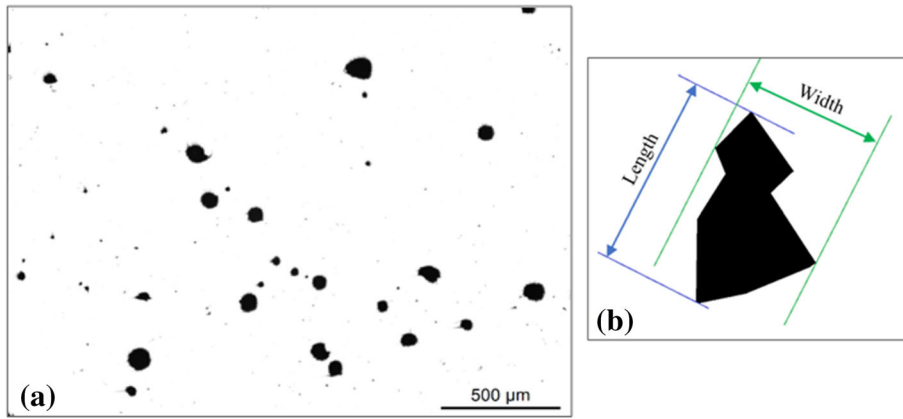


Fig. 18 (a), (b) Binarized optical microscope image for image analysis and graphical representation of length and width of pores according to (Ref 49)

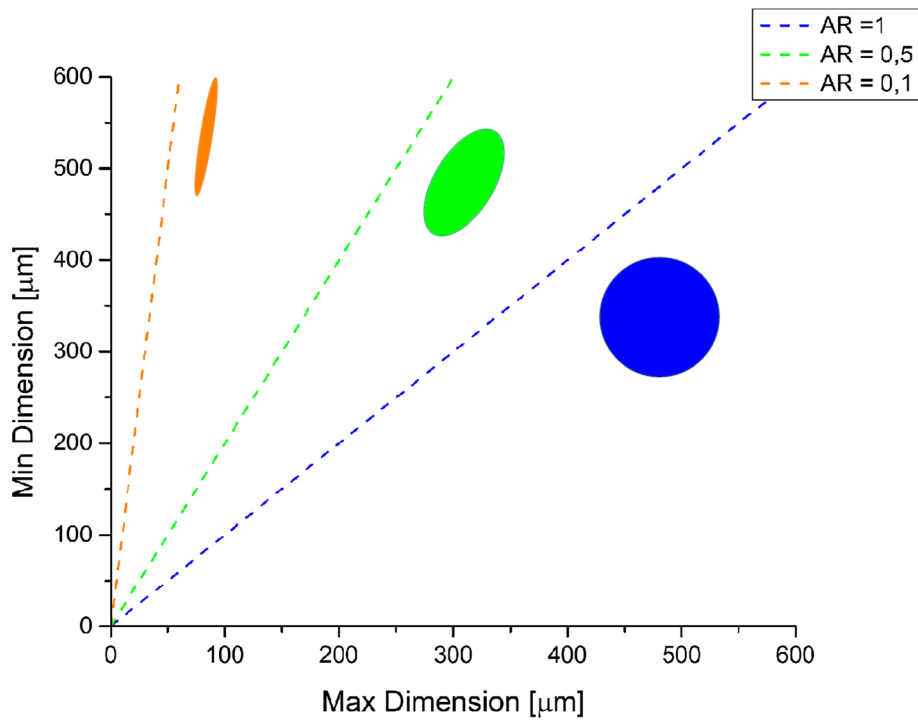


Fig. 19 Graphical representation of the aspect ratio equal to 1 (blue line), 0.5 (green line) and 0.1 (orange line) to clarify Fig. 12 (Color figure online)

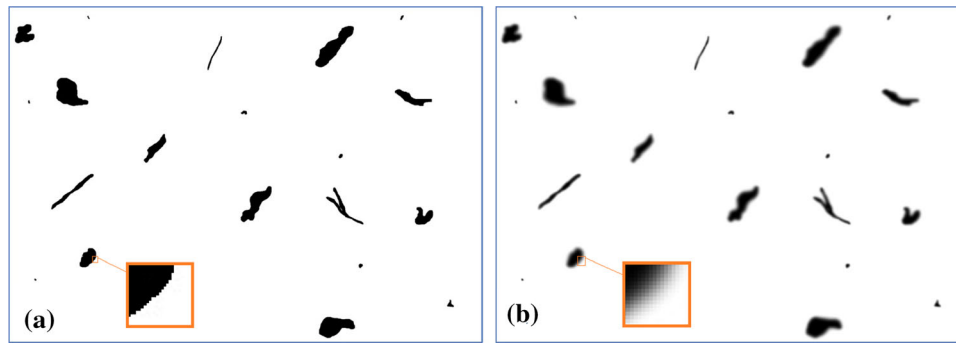


Fig. 20 Drawn image to evaluate the error contribution that can be caused by the operator during image analysis: (a) clear image; (b) blurred image

Acknowledgment

The authors would like to thank BeamIT S.p.A. (Fornovo di Taro Parma, Italy) for providing the samples employed in this study.

Open Access

This article is licensed under a Creative Commons Attribution 4.0 International License, which permits use, sharing, adaptation, distribution and reproduction in any medium or format, as long as you give appropriate credit to the original author(s) and the source, provide a link to the Creative Commons licence, and indicate if changes were made. The images or other third party material in this article are included in the article's Creative Commons licence, unless indicated otherwise in a credit line to the material. If material is not included in the article's Creative Commons licence and your intended use is not permitted by statutory regulation or exceeds the permitted use, you will need to obtain permission directly from the copyright holder. To view a copy of this licence, visit <http://creativecommons.org/licenses/by/4.0/>.

Data Availability

The processed data required to produce these results cannot be shared at this time because these are also considered in an ongoing study.

Appendix A

The pores' analysis was conducted according to ISO 46655-1:2014, and the measurements have been systematically performed on 6 micrographs at a magnification of $100\times$ (Fig. 18a) analyzing a total area of $24,936.41 \times 10^3 \mu\text{m}^2$ for each sample studied. The maximum and minimum dimension of each pore and its roundness were considered to evaluate the effect of T6 heat treatment. In the first case, the maximum and minimum dimensions (Fig. 18b) represent the greatest (maximum Feret diameter) and the shortest (minimum Feret diameter) distance between parallel lines drawn through 2 points on a feature's boundary regardless of orientation, as textually reported in (Ref 51). The ratio between the minimum and maximum Feret diameters defines the aspect ratio (AR) of the object analyzed. Figure 10 illustrates the aspect ratio

variation in all pores before and after the T6 heat treatment performed on bars manufactured via single- and dual-laser machine setup. In all graphs shown, the y- and x-axes represent the minimum and maximum dimensions, respectively, of all pores, while black and red lines the Linear Fits obtained by selecting all points and applying the automatical analysis of OriginPro 9.0.0 software. The same method was used to determine the square of the Pearson correlation coefficient (R^2).

At the same time, the blue, green and orange dotted lines were drawn considering the aspect ratios of 1, 0.5 and 0.1, respectively. For the three different lines, the following equations were considered:

$$y = x \quad (\text{Eq 7})$$

where y and x represent the minimum and maximum dimensions, respectively. Figure 19 clarifies the interpretation of the plots reported in Fig. 10 showing a graphic schematization of the typical morphology in relation to the aspect ratio (AR) of pores (Ref 51). The blue dotted line is referred to the AR equal to 1 (maximum dimension coinciding with the minimum dimension), while the green and orange dotted lines to AR are equal to 0.5 and 0.1, respectively. These last functions are described by Eq 9 and 10:

$$y = 2x \quad (\text{Eq 8})$$

$$y = 10x \quad (\text{Eq 9})$$

In the second case, the roundness (R) is defined as follows:

$$R = \frac{4\pi A}{p^2} \quad (\text{Eq 10})$$

where A and p are the area and the perimeter of the objects analyzed through the image analysis. The object is a circle if the $R \rightarrow 1$, while it becomes less round of $R \rightarrow 0$ (Ref 51).

Another considered parameter is the equivalent diameter defined as the diameter of a circle that is characterized by the same area of the object analyzed (Ref 51).

The average values of the pore per area [$\mu\text{m}^2/\text{pore}$] were obtained as:

$$a = \frac{\sum_i (A_p)_i}{M} \quad (\text{Eq 11})$$

where A_p is the area of a single analyzed pore and M is the total pore's number.

The sample relative density was defined as follows:

$$\rho = 1 - \frac{\sum_i (A_p)_i}{\sum_{j=1}^6 \hat{A}_j} \quad (\text{Eq 12})$$

where $\sum_{j=1}^6 \hat{A}_j$ is the area of the 6 micrographs analyzed for each sample, i.e., $24,936.41 \times 10^3 \mu\text{m}^2$.

The standard errors ($\sigma_{\bar{x}}$) associated with pore area and consequently to the sample density were calculated by adding two contributions: one related to the operator and one to the OM device.

The first contribution was calculated by comparing the objects' areas contained into two images shown in Fig. 20(c), (d). The first image (Fig. 20c) was drawn through GIMP Image Manipulation Program to represent a micrograph with different kinds of pores (black objects) in terms of size, morphology and area which was calculated through the automatic image analysis. These real areal values are obtained by selecting the only black pixels given that there is a perfect distinction between the central and external areas of the black object (orange panel in Fig. 20c). The second one (Fig. 20d) shows the same image in Fig. 20(c) but with pore boundaries that were artificially blurred to represent the real work conditions found during the manual image analysis. As matter of fact, analyzing the high magnification optical micrographs, the pore boundaries appear blurred as represented in the orange panel in Fig. 20(d).

For evaluating the standard errors associated with each pore area, the automatic image analysis is carried out in Fig. 20(c), while the manual image analysis is performed in Fig. 18(d) to evaluate the areas of the blurred black objects. This image was analyzed 20 times to obtain a good statistical population. So, the standard errors ($\sigma_{\bar{x}} = \sigma/\sqrt{N}$) were calculated through the standard deviation (σ) and the N observations and, subsequently, associated with the pore area as shown in Table 6.

By the fact that the standard errors were associated with the pore areas, it is necessary calculated an error (e_a) that will be associated with the density values, as follows:

$$e_a = \frac{\rho_{\max} - \rho_{\min}}{2} = \frac{\left[\left(1 - \frac{\sum_i (A_p)_i}{\sum_{j=1}^6 \hat{A}_j} \right)_{\min} \right] - \left[\left(1 - \frac{\sum_i (A_p)_i}{\sum_{j=1}^6 \hat{A}_j} \right)_{\max} \right]}{2} \quad (\text{Eq 13})$$

where ρ is the relative density, and \hat{A}_j is the micrograph area (μm^2). $\left[\left(\frac{\sum_i (A_p)_i}{\sum_{j=1}^6 \hat{A}_j} \right)_{\max} \right]$ and $\left[\left(\frac{\sum_i (A_p)_i}{\sum_{j=1}^6 \hat{A}_j} \right)_{\min} \right]$ are the overestimation and the underestimation of the total pore areas calculated applying the standard errors shown in Table 6.

References

- W. Li, S. Li, J. Liu, A. Zhang, Y. Zhou, Q. Wei, C. Yan and Y. Shi, Effect of heat treatment on AlSi10Mg Alloy Fabricated by Selective Laser Melting, Microstructure Evolution, Mechanical Properties and Fracture Mechanism, *Mater. Sci. Eng.*, 2016, **663**, p 116–125. <https://doi.org/10.1016/j.msea.2016.03.088>
- A. Mertens, J. Delahaye, O. Dedry, B. Vertruyen, J. Tchuindjang and A. Habraken, Microstructure and Properties of SLM AlSi10Mg, Understanding the Influence of Local Thermal History, *Proc. Manuf.*, 2020, **47**, p 1089–1095. <https://doi.org/10.1016/j.promfg.2020.04.121>
- M. Cabrini, F. Calignano, P. Fino, S. Lorenzini, M. Lorusso, D. Manfredi, C. Testa and T. Pasatore, Corrosion Behaviour of Heat-

Treated AlSi10Mg Manufactured by Laser Powder Bed Fusion, *Mater.*, 2018, **11**(7), p 1051. <https://doi.org/10.3390/ma11071051>

- X. Cao and J. Campbell, Morphology of β -Al₅FeSi Phase in Al-Si Cast Alloys, *Mater. Trans.*, 2006, **47**(5), p 1303–1312. <https://doi.org/10.2320/matertrans.47.1303>
- E. Cerri, E. Ghio and G. Bolelli, Effect of Distance From Build Platform and the Post-heat Treatment of AlSi10Mg Alloy Manufactured by Single and Multi-laser SLM, *JMEP*, 2021, **30**(8), p 4981–4992. <https://doi.org/10.1007/s11665-021-05577-8>
- C. Yap, C. Chua, Z. Dong, Z. Liu, D. Zhang, L. Loh and S. Sing, Review of Selective Laser Melting: Materials and Applications, *Phys. Rev. Appl.*, 2015, **2**, 041101. <https://doi.org/10.1063/1.4935926>
- X.J. Wang, L.C. Zhang, M.H. Fang and T.B. Sercombe, The Effect of Atmosphere on the Structure and Properties of a Selective Laser Melted Al-12Si Alloy, *Mater. Sci. Eng. A.*, 2014, **597**, p 370–375. <https://doi.org/10.1016/j.msea.2014.01.012>
- H. Heyr, L. Zhou, S. Park, G. Gottsfritz, G. Benson, B. Tolentino, B. McWilliams, K. Cho and Y. Sohn, Understanding the Laser Powder Bed Fusion of AlSi10Mg Alloy, *Metallogr. Microstruct. Anal.*, 2020, **9**, p 484–502. <https://doi.org/10.1007/s13632-020-00659-w>
- N. Aboulkhair, N. Everitt, I. Ashcroft and C. Tuck, Reducing Porosity in AlSi10Mg Parts Processed by Selective Laser Melting, *Addit. Manuf.*, 2014, **1–4**, p 77–86. <https://doi.org/10.1016/j.addma.2014.08.51>
- M. Tang, P. Pistorius, J. Beuth, Geometric model to predict porosity of part produced in powder bed system, in *Materials Science & Technology conference and exhibition*, Columbus, Ohio, USA, 2015
- S. Bai, N. Parevoshchikova, Y. Sha and X. Wu, The Effects of Selective Laser Melting Process Parameters on Relative Density of the AlSi10Mg Parts and Suitable Procedures of the Archimedes Method, *App. Sci.*, 2019, **9**(3), p 583. <https://doi.org/10.3390/app9030583>
- I. Anderson, M. White and R. Dehoff, Feedstock Powder Processing Research Needs for Additive Manufacturing Development, *Curr. Opin. Solid State Mater. Sci.*, 2018, **22**(1), p 8–15. <https://doi.org/10.1016/j.cossms.2018.01.002>
- Y. Shi, K. Yang, S. Kairy, F. Palm, X. Wu and P. Rometsch, Effect of Platform Temperature on Porosity, Microstructure and Mechanical Properties of an Al-Mg-Cu-Zn Alloy Fabricated by Selective Laser Melting, *Mater. Sci. Eng. A.*, 2018, **732**, p 41–52. <https://doi.org/10.1016/j.msea.2018.06.049>
- J. Tiwari, A. Mandal, N. Sathish, A. Agrawal and A. Srivastava, Investigation of Porosity, Microstructure and Mechanical Properties of Additively Manufactured Graphene Reinforced AlSi10Mg Composite, *Addit. Manuf.*, 2020, **33**, 101095. <https://doi.org/10.1016/j.addma.2020.101095>
- J. Damon, S. Dietrich, F. Vollert, J. Gibmeier and V. Schulze, Process Dependent Porosity and Influence of Shot Penning on Porosity Morphology Regarding Selective Laser Melted AlSi10Mg Parts, *Addit. Manuf.*, 2018, **20**, p 77–89. <https://doi.org/10.1016/j.addma.2018.01.001>
- Z. Xu, W. Wen and T. Zhai, Effects of Pore Position in Depth on Stress/Strain Concentration and Fatigue Crack Initiation, *Metall. Mater. Trans.*, 2012, **43**, p 2763–2770. <https://doi.org/10.1007/s11661-011-0947-x>
- T. Davis, D. Healy, A. Bubeck and R. Walker, Stress Concentrations Around Voids in Three Dimensions: The Roots of Failure, *JSG*, 2017, **102**, p 193–207. <https://doi.org/10.1016/j.jsg.2017.07.013>
- E. Ghio and E. Cerri, Work Hardening of Heat-Treated AlSi10Mg Alloy Manufactured by Single and Double Laser Selective Laser Melting: Effects of Layer Thickness and Hatch Spacing, *Mater.*, 2021, **14**(17), p 4901–4924. <https://doi.org/10.3390/ma14174901>
- B. Chen, S. Moon, X. Yao, G. Bi, J. Shen, J. Umeda and K. Kondoh, Strength and Strain Hardening of Selective Laser Melted AlSi10Mg Alloy, *Scr. Mater.*, 2017, **141**, p 45–49. <https://doi.org/10.1016/j.scripta.2017.07.025>
- C. Zhang, H. Zhu, Z. Hu, L. Zhang and X. Zeng, A Comparative Study on SINGLE-LASER And Multi-Laser Selective Laser Melting AlSi10Mg: Defects, Microstructure and Mechanical Properties, *Mater. Sci. Eng. A.*, 2019, **746**, p 416–423. <https://doi.org/10.1016/j.msea.2019.01.024>
- P. Van Cauwenbergh, V. Samaee, L. Thijs, J. Nejezchlebová, P. Sedláč, A. Iveković, D. Schyvers, B. Van Hooreweder and K. Vanmeensel, Unravelling the Multi-Scale Structure-Property Relationship of Laser

- Powder Bed Fusion Processed and Heat-Treated AlSi10Mg, *Sci. Rep.*, 2021, **11**, p 6423. <https://doi.org/10.1038/s41598-021-85047-2>
22. D. Dai, D. Gu, R. Poprawe and M. Xia, Influence of Additive Multilayer Feature on Thermodynamics, Stress and Microstructure Development during Laser 3D Printing of Aluminium-Based Material, *Sci. Bull.*, 2017, **67**(11), p 779. <https://doi.org/10.1016/j.scib.2017.05.007>
 23. R. Casati, M. Nasab, M. Coduri, V. Tirelli and M. Vedani, Effect of Platform Pre-heating and Thermal Treatments Strategy on Properties of AlSi10Mg Alloy Processed by Selective Laser Melting, *Metals*, 2018, **8**, p 954–966. <https://doi.org/10.3390/met8110954>
 24. T. Yang, T. Liu, W. Liao, E. MacDonald, H. Wei, C. Zhang, X. Chen and K. Zhang, Laser Powder Bed Fusion of AlSi10Mg: Influence of Energy Intensities on Spatter and Porosity Evolution, Microstructure and Mechanical Properties, *J. Alloy Compd.*, 2018, **849**, 156300. <https://doi.org/10.1016/j.jallcom.2020.156300>
 25. A. Singla, M. Banerjee, A. Sharma, J. Singh, A. Bansal, M. Gupta, N. Khanna, A. Shahi and D. Goyal, Selective Laser Melting of Ti6Al4V alloy: Process Parameters, Defects and Post-Treatments, *J. Manuf. Process.*, 2021, **64**, p 161–187. <https://doi.org/10.1016/j.jmapro.2021.01.009>
 26. C. Rakesh, N. Priyanka, R. Jayaganthan and N. Vasa, Effect of Build Atmosphere on the Mechanical Properties of AlSi10Mg Produced by Selective Laser Melting, *Mater. Today. Commun.*, 2018, **5**(9), p 17231–17238. <https://doi.org/10.1016/j.matpr.2018.04.133>
 27. M. Tiryakioglu, The Effect of Hydrogen on Pore Formation in Aluminium Alloy Castings: Myth Versus Reality, *Metals*, 2020, **10**, p 368.
 28. C. Weingarten, D. Buchbinder, N. Pirch, W. Meiners, K. Wissenbach and R. Poprawe, Formation and Reduction of Hydrogen Porosity during Selective Laser Melting of AlSi10Mg, *JMPPT*, 2015, **221**, p 112–120. <https://doi.org/10.1016/j.jmatprotec.2015.02.013>
 29. Y. Li and D. Gu, Parametric Analysis of Thermal Behavior During Selective Laser Melting Additive Manufacturing of Aluminum Alloy Powder, *Mat. Des.*, 2014, **63**, p 856–867. <https://doi.org/10.1016/j.matdes.2014.07.006>
 30. N. Aboulkhair, I. Maskery, C. Tuck, I. Ashcroft and N. Everitt, The microstructure and Mechanical Properties of Selective Laser Melted AlSi10Mg: The Effect of CONVENTIONAL T6-like Heat Treatment, *Mater. Sci. Eng. A.*, 2016, **667**, p 139–143. <https://doi.org/10.1016/j.msea.2016.04.092>
 31. E. Brandl, U. Heckenberger, V. Holzinger and D. Buchbinder, Additive Manufactured AlSi10Mg Samples Using Selective Laser Melting: Microstructure, High Cycle Fatigue, and Fracture Behaviour, *Mater. Des.*, 2012, **34**, p 159–169. <https://doi.org/10.1016/j.matdes.2011.07.067>
 32. D. Buchbinder, H. Schleifenbaum, S. Heidrick, W. Meines and J. Bueltmann, High Power Selective Laser Melting (HIP SLM) of Aluminium Part, *Phys. Procedia.*, 2011, **121**, p 271–278. <https://doi.org/10.1016/j.phpro.2011.03.035>
 33. K. Kempen, L. Thijs, J.V. Humbeeck and J.P. Kruth, Processing AlSi10Mg by Selective Laser Melting: Parameter Optimization and Material Characterization, *Mater. Sci. Technol.*, 2015, **31**, p 917–923. <https://doi.org/10.1179/1743284714Y.0000000702>
 34. N. Read, W. Wang, K. Essa and M.M. Attallah, Selective Laser Melting of AlSi10Mg Alloy: Process Optimization and Mechanical Properties Development, *Mater. Des.*, 2015, **65**, p 417–424. <https://doi.org/10.1016/j.matdes.2014.09.044>
 35. Z.H. Xiong, S.L. Liu, S.F. Li, Y. Shi, Y.F. Yang and R.D.K. Misa, Role of Melt Pool Boundary Condition in Determining the Mechanical Properties of Selective Laser Melting AlSi10Mg Alloy, *Mater. Sci. Eng. A.*, 2019, **740–741**, p 148–156. <https://doi.org/10.1016/j.msea.2018.10.083>
 36. Y. Bai, Y. Yang, Z. Xiao, M. Zhang and D. Wang, Process Optimization and mechanical property Evolution of AlSiMg0.75 Selective Laser Melting, *Mater. Des.*, 2018, **140**, p 257–266. <https://doi.org/10.1016/j.matdes.2017.11.045>
 37. F. Uriati, F. Betta, P. Ferro, S. Rosso, G. Savio, G. Concheri, R. Meneghello, High density AlSi10Mg aluminium alloy specimens obtained by selective laser melting, in *International conference on Design, Simulation, Manufacturing: The Innovation Exchange*, Modena, Italy, 2019
 38. A. Majeed, Y. Zhang, J. Lv, T. Peng, Z. Atta and A. Ahmed, Investigation of T4 and T6 Heat Treatment Influences on Relative Density and Porosity of AlSi10Mg Alloy Components Manufactured by SLM, *Comput. Ind. Eng.*, 2020, **139**, 106194. <https://doi.org/10.1016/j.cie.2019.106194>
 39. L. Girelli, M. Tocci, M. Gelfi and A. Pola, Study of Heat Treatment Parameters for Additively Manufactured AlSi10Mg in Comparison with Corresponding Cast Alloy, *Mat. Sci. Eng. A*, 2019, **739**, p 317–328. <https://doi.org/10.1016/j.msea.2018.10.026>
 40. B. Zhang, W.J. Meng, S. Shao, N. Phan and N. Shamsaei, Effect of Heat Treatments on Pore Morphology and Microstructure of Laser Additively Manufactured Parts, *Mater. Des. Process. Commun.*, 2019 <https://doi.org/10.1002/mdp2.29>
 41. A. Chajjaruwanch, P. Lee, R. Dashwod, Y. Yousef and H. Nagaumi, Evolution of Pore Morphology and Distribution During the Homogenization of Direct Chill Cast Al-Mg Alloys, *Acta Mater.*, 2007, **55**(1), p 285–293. <https://doi.org/10.1016/j.actamat.2016.08.023>
 42. J. Gu, S. Yang, M. Gao, J. Bai, Y. Zhai and J. Ding, Micropore Evolution in Additively Manufactured Aluminium Alloys under Heat Treatment and Inter-Layer Rolling, *Mat. Des.*, 2020, **186**, 108228. <https://doi.org/10.1016/j.matdes.2019.108288>
 43. L.F. Wang, J. Sun, X.L. Yu, Y. Shi, X.G. Zhu, L.Y. Cheng, H.H. Liang, B. Yan and L.J. Guo, Enhancement in Mechanical Properties of Selectively Laser-Melted AlSi10Mg Aluminium Alloy by T6-like Heat Treatment, *Maer. Sci. Eng. A.*, 2018, **734**, p 299–310. <https://doi.org/10.1016/j.msea.2018.07.103>
 44. A. Maamoun, Y. Xue, M. Elbestawi and S. Veldhuis, Effect of Selective Laser Melting Process Parameters on Quality of Al Alloy Parts: Powder Characterization, Density, Surface Roughness, and dimensional accuracy, *Materials*, 2018, **11**(12), p 2343. <https://doi.org/10.3390/ma11122343>
 45. X. Teng, G. Zhang, J. Liang, H. Li, Q. Liu, Y. Cui, T. Cui and L. Jiang, Parameter Optimization and Microhardness Experiment of AlSi10Mg Alloy Prepared by Selective Laser Melting, *Mater. Res. Express*, 2019, **6**(8), 086592. <https://doi.org/10.1088/2053-1591/ab18d0>
 46. Z. Li, Z. Li, Z. Tan, D.-B. Xiong and Q. Guo, Stress Relaxation and the Cellular Structure-Dependence of Plastic Deformation in Additively Manufactured AlSi10Mg Alloys, *Int. J. Plast.*, 2020, **127**, 102640. <https://doi.org/10.1016/j.ijplas.2019.12.003>
 47. L. Zhao, J.G.S. Macias, L. Ding, H. Idrissi and A. Simar, Damage Mechanisms in Selective Laser Melted AlSi10Mg under as Build and Different Post-process Conditions, *Mater. Sci. Eng. A.*, 2019, **764**, p 138210.
 48. B. Chen, S.K. Moo, X. Yao, G. Bi, J. Shen, J. Umeda and K. Kondoh, Strength and Strain Hardening of Selective Laser Melted AlSi10Mg Alloy, *Ser. Mater.*, 2017, **141**, p 45–49. <https://doi.org/10.1016/j.scripta.mat.2017.07.025>
 49. H. Gong, K. Rafi, H. Gu, G.D. Janaki Ram, T. Starr and B. Stucker, Influence of Defects on Mechanical Properties of Ti-6Al-4V Components Produced by Selective Laser Melting and Electron Beam Melting, *Mater. Des.*, 2015, **86**, p 545. <https://doi.org/10.1016/j.matdes.2015.07.147>
 50. J.C. Hastie, J. Koolbin, M.E. Karol, M.M. Attallah and R. Martinez, Evolution of Internal Pores within AlSi10Mg Manufactured by Laser Powder Bed Fusion Under Tension: As-Built and Heat Treated Conditions, *Mater. Des.*, 2021, **204**, 109645. <https://doi.org/10.1016/j.matdes.2021.109645>
 51. L. Mycosystems, *Measurement Parameter Description*, in *LAS AF 2D Analysis*, Mannheim, Germany, 2014, p 113–116

Publisher's Note Springer Nature remains neutral with regard to jurisdictional claims in published maps and institutional affiliations.